



Delft University of Technology

Torque model verification for the GOCE satellite

Visser, Tim; Doornbos, Eelco; de Visser, Coen; Visser, Pieter; Fritsche, Bent

DOI

[10.1016/j.asr.2018.06.025](https://doi.org/10.1016/j.asr.2018.06.025)

Publication date

2018

Document Version

Accepted author manuscript

Published in

Advances in Space Research

Citation (APA)

Visser, T., Doornbos, E., de Visser, C., Visser, P., & Fritsche, B. (2018). Torque model verification for the GOCE satellite. *Advances in Space Research*, 62(5), 1114-1136. <https://doi.org/10.1016/j.asr.2018.06.025>

Important note

To cite this publication, please use the final published version (if applicable). Please check the document version above.

Copyright

Other than for strictly personal use, it is not permitted to download, forward or distribute the text or part of it, without the consent of the author(s) and/or copyright holder(s), unless the work is under an open content license such as Creative Commons.

Takedown policy

Please contact us and provide details if you believe this document breaches copyrights. We will remove access to the work immediately and investigate your claim.

Torque model verification for the GOCE satellite

Tim Visser*, Eelco N. Doornbos*, Coen C. de Visser*, Pieter N.A.M. Visser*

*Delft University of Technology, Faculty of Aerospace Engineering, Kluyverweg 1, 2629
HS Delft, The Netherlands*

Bent Fritsche*

Hyperschall Technologie Göttingen GmbH, Katlenburg-Lindau, Germany

Abstract

The modeling of torques acting on satellites is essential for the design of satellite attitude control systems. The GOCE satellite, equipped with accurate accelerometers, star trackers and GPS receivers, presents an opportunity to validate these models. Although the forces on GOCE and other accelerometer-carrying missions have been extensively analyzed in the past, a similar analysis has so far not yet been made for the torques.

In this paper, we present a set of torque models for the GOCE satellite. It consists of six main parts: 1) magnetic torquer actuators, 2) aerodynamic torque, 3) gravity gradient torque, 4) solar radiation pressure torque, 5) thruster torque, and 6) passive magnetic torque. The magnetic properties of the payload are approximated using a parametrization, of which the parameters are estimated from the observation data.

Based on data recorded during selected spacecraft events, the model for the control torques can be validated and error sources are identified in the other models. The models perform best in roll and pitch, where the standard deviation is reduced to 15.2% and 2.1% of the standard deviation of the control torque around those axes respectively. In yaw the standard deviation is significantly larger at 30.5%. The remaining differences between models and

*Corresponding author:

Email addresses: t.visser-1@tudelft.nl (Tim Visser),
e.n.doornbos@tudelft.nl (Eelco N. Doornbos), c.c.devisser@tudelft.nl
(Coen C. de Visser), p.n.a.m.visser@tudelft.nl (Pieter N.A.M. Visser),
b.fritsche@htg-hst.de (Bent Fritsche)

observations show magnetic signatures due to electric currents and signatures of aerodynamic model errors. The latter correspond well with an increase in thermosphere density and wind speed with increased geomagnetic activity. The pitch torque is found to be a potential source of vertical wind data.

Keywords: Satellite torque modeling, Gravity field and steady-state Ocean Circulation Explorer (GOCE), Satellite aerodynamics, Magnetic attitude control

1. Introduction

The goal of this paper is to test the validity of torque models for the Gravity field and steady-state Ocean Circulation Explorer (GOCE) satellite, by comparing the individually modeled torques with total torques obtained from the angular accelerations that were measured on the satellite. The models that are investigated represent the aerodynamic, radiation pressure, gravity gradient, magnetic and actuator torques. Second, we demonstrate that models and measurements of torques on GOCE are important for improving our understanding of satellite aerodynamics and investigating thermosphere density and wind. The further pursuit of these goals will be the subject of future work.

GOCE was a unique satellite. Its highly accurate measurements and low orbit are especially suitable for analyses of aerodynamic forces and torques. However, this does not mean that the results of this paper are only applicable to GOCE. In fact, in our conclusions and recommendations, we will discuss the extent to which the models can be applied to both existing satellite missions and concepts for future missions in low Earth orbit, and how data from such other satellites could be applied for the same goals.

This work is motivated by the need to resolve outstanding issues in the field of satellite aerodynamics and related discrepancies between datasets and models of thermosphere dynamics. Since the early days of spaceflight, analyses of accelerations on satellites in low Earth orbit have been used to derive observation data of the thermosphere (e.g. King-Hele, 2005). With the near-continuous operation of space-based accelerometers in polar low Earth orbits, provided by CHAMP, GRACE, GOCE and Swarm, this domain has received a strong boost, leading to a significant increase in publications on thermosphere dynamics and improvements of thermosphere models (see e.g. Doornbos (2011); Emmert (2015); Visser et al. (2013) and references

therein). In all recent studies using these satellites, only linear acceleration measurements have been used, even though the star camera and accelerometer measurements also contain information on angular accelerations. The main argument for not using these is most likely that the angular acceleration measurements are more contaminated by non-aerodynamics signals than their linear counterparts, such as magnetic perturbations and control activities.

The most important limitations in the thermosphere datasets resulting from these missions are due to the use of approximative satellite geometry models and assumptions made in the gas-surface interaction models used to describe the satellite aerodynamic interaction. This is a fairly complex multi-disciplinary topic, and these limitations might not be immediately obvious to users of the affected data. The most obvious indications of such limitations might be found in the form of scale differences between the density data sets of different missions and models (Doornbos, 2011, section 5.3), and discrepancies between the accelerometer-derived and ground-based wind measurements, especially at high latitudes (Kärräng, 2015; Dhadly et al., 2017). It is likely that there are also more subtle consequences, and it is certain that such problems in the models used in the processing mix with any data-related problems and thereby limit our ability to disentangle, model and remove them.

Among the previous work done to increase the fidelity of the accelerometer data processing is the application of non-hyperthermal satellite aerodynamics (Koppenwallner, 2008; Sutton, 2009; Doornbos, 2011), the development of an attitude-independent algorithm that properly takes into account lift and wind (Doornbos et al., 2010), empirical modeling of gas-surface interaction parameters (Pilinski et al., 2013a; Walker et al., 2014) and development of high-fidelity satellite geometry models (Mehta et al., 2014, 2017). However, due to the sparsity of data, so far these efforts have undergone only limited validation. So far, these data processing developments have not been applied to all modern accelerometer satellites in the same way, making it difficult to further investigate inconsistencies. Finally, the empirical gas-surface parameter modeling efforts are based on old and sparse data on aerodynamic forces and torques, on so-called paddlewheel satellites, that were flown in the late 1960s and early 1970s (Pilinski et al., 2013b). Due to the obscurity of the paddlewheel data and associated mission documentation, it is difficult to assess their accuracy and impossible to replicate these studies from scratch.

The high cadence and accurate angular acceleration measurements by

GOCE are a readily available additional data source for this line of investigation. Along with housekeeping data that enables accurate torque modeling, it is our intention that this modern dataset will augment or replace the paddlewheel satellite analyses, to provide new insights on satellite aerodynamics and thermosphere variability.

The data processing and modeling work presented here has value in the engineering as well as the scientific domain. Models of torques on satellites (e.g. Wertz, 1978; Wie, 2008) are crucial for the design and scaling of spacecraft attitude control subsystems, and have therefore been tested extensively by indirect methods, i.e. by assessing whether these systems are capable of maintaining the desired attitude pointing and maintaining desired angular rates. However, a direct and precise comparison of modeled torques and observed angular accelerations has, to the best of our knowledge, not been published before.

The paper describes how the torque models from the engineering literature cited above have been adapted for the GOCE satellite. To validate the torque models, we have first calculated a *measured torque* from the measured angular rate, angular acceleration, and satellite inertia matrix. In the next step, all models have been evaluated and summed to come to a total of the directly modeled torque. Because the magnetic properties of the satellite payload are not known to us, an extra set of magnetic dipoles was estimated for each day from the residual torque. A linear fit was made to the daily estimates, from which the dipole at each time instance was obtained. The torque caused by these dipoles was added to the total modeled torque. To validate the complete set of models the two results were compared and their differences were examined for signatures that point to specific model errors. The control torque was individually validated by investigating the model error over an episode of increased control activity.

The result of this endeavor is a complete, validated set of torque models for the GOCE satellite. This result is generalized to other low Earth orbiting satellites by identifying the magnitude and source of the main model errors. Most notably, the pitch and especially the yaw residual show significant signatures that point to aerodynamic torque modeling errors.

The paper is structured as follows: First in Section 2, the data sources are presented, as well as the Earth models used and the reference frames in which these data are defined. Then in section 3, the model definitions are provided for each source of torque. The procedure of estimating payload dipoles is described in Section 3.6. In Section 4, the validation of each indi-

vidual contribution to the total torque is discussed. Finally the conclusions of this work are provided in Section 5, where the possibility of extracting aerodynamic and thermospheric information from the torque residuals is further discussed, as well as implications for other existing missions and future mission concepts.

2. The GOCE mission and datasets

The GOCE satellite (Gravity field and steady-state Ocean Circulation Explorer) (Drinkwater et al., 2003; Fehring et al., 2008; Floberghagen et al., 2011) was launched on 17 March 2009 for the purpose of mapping the static part of the Earth’s gravity field at high spatial resolution. This improved gravity field mapping capability has many application areas, including the investigation of ocean circulation patterns. As its main instruments, the satellite carried GPS receivers for satellite-to-satellite tracking and a gradiometer to measure gravity gradients. An ion engine, driven by solar power and Xenon fuel, was used to provide a quiet environment for the accelerometers and counteract orbit decay due to drag to maintain a very low mean altitude (below 270 km).

A set of star trackers was used for attitude determination. In order to minimize disturbances of the gradiometer readings, attitude control in science mode was implemented using three magnetic torquer actuators only. Four fins on the top, bottom, and back of the satellite were designed for additional aerodynamic stability (see Fig. 1). Three 3D fluxgate magnetometers were available as sensors in the AOCS subsystem, in addition to the star trackers.

A near-polar, near sun-synchronous dusk-dawn orbit with 96.7° inclination was selected to maximize available solar power and achieve near-global coverage. After depletion of the Xenon fuel on October 22, 2013, the orbit underwent natural decay, after which the satellite broke up during re-entry over the South-Atlantic on November 11, after more than 4.5 years of successful operations (GOCE Flight Control Team (HSO-OEG), 2014).

The Electrostatic Gravity Gradiometer (EGG) instrument on-board GOCE consisted of six individual accelerometers that each measured the linear accelerations in all three principle body-fixed axis directions. The gravity gradients, as well as the linear non-gravitational accelerations and angular accelerations can be derived by taking specific combinations of these individual measurements (Rummel et al., 2011).



Figure 1: Artist impression of the GOCE satellite in orbit. Courtesy of ESA/AOES Medialab.

In preparation for the creation of the torque model, all relevant data and documentation were acquired. This included finding information on the positioning and magnetic properties of the satellite parts in the mission documentation. These data were then implemented in a custom made Matlab toolbox in which the measured and modeled torques were calculated. As the magnetic properties of the payloads were not available, additional hard magnetic and soft magnetic dipoles were estimated, reducing the residual, unmodeled torque in a weighted least squares sense. This was done for the complete science phase of the mission. Periods for which the data are deemed of insufficient quality, as reported by ESA, were excluded.

For each model an attempt was made to isolate a short part of the mission in which that torque was dominant, changing abruptly, or known a priori. This approach has led to the validation of most parts of the individual models. Finally the sum of the torque model output was compared to the measured torque over the entire mission, resulting in the validation of the model as a whole.

In the presented analysis, five different reference frames are used. They

are listed in Table 1, along with the abbreviations used in the remainder of this paper. All analyses are performed in the body (B) frame. The orbital (O) frame is used only to define Euler attitude angles, since the attitude control was designed to keep the satellite body axes aligned with respect to the orbital velocity and orbital angular momentum vector directions. The other frame definitions in Table 1 are used to convert measurements and model outputs to the B-frame.

For the analysis of the torques acting on GOCE, both scientific data products and housekeeping data are required. A list of the data used is provided in Table 2. Note that the reference frame symbols refer to Table 1. Of the EGG_NOM and SST_PSO products we use version 5.06. A recent reprocessing effort by Siemes (2018) suggests that the calibration of this data may be improved in a future release.

The Earth models used in the analysis are listed in Table 3. The International Geomagnetic Reference Field (IGRF) is only used to calibrate the magnetometer readings, whereas the other models are used in torque calculations directly. NRLMSISE-00 is only used to calculate the local temperature and the number density of thermospheric constituents. At GOCE’s altitude the main contributions to drag will be due to oxygen and nitrogen, which have similar molecular mass. Errors in the atmospheric composition will therefore have a limited effect on the aerodynamic coefficients (see Fig. 3.9 in Doornbos (2011)). The number densities are scaled with the ratio of density from NRLMSISE-00 to the density estimated from the linear accelerations of GOCE (Doornbos, 2016). The latter data is also the source for horizontal wind. Vertical wind is not modeled.

Table 3: The models used in the data analysis and calibration.

Input	Model	Output
Orbit	IGRF	Magnetic field
Orbit, time, ap, F10.7	NRLMSISE-00	Number densities, temperature
Time	GOCE+ Thermospheric Data ^a	Neutral density, cross-wind

^a Thermospheric density and cross-wind derived from GOCE linear accelerations by Doornbos (2016).

For the analysis of the data the argument of latitude is used to describe the progress of the satellite in its orbit. This parameter runs from 0 to 360 degrees for each orbit, with the origin defined at the ascending node. For GOCE, which was in a near-circular, near-polar orbit, this parameter is

Table 1: Reference frame definitions, all right-handed.

Frame	Origin	x	y	z
Inertial	Earth's center of mass	Mean equinox	(-)	Earth's rotation axis
Earth fixed	Earth's center of mass	Greenwich meridian	(-)	Earth's rotation axis
Spacecraft	Reference point on back plate	Forward (symmetry axis)	(-)	Main fin (nadir)
Body	Satellite center of mass	Forward (symmetry axis)	(-)	Main fin (nadir)
Orbital	Satellite center of mass	Velocity (Earth's surface)	Angular momentum	(-)
Local NED	Satellite center of mass	North	East	Down

Table 2: Overview of used science (above) and housekeeping data (below the line).

Data	Product	Field	Unit	Rate [Hz]	Frame
Orbit and velocity	SST_PSO	PRD	km, dm/s	1/10	E
Earth's orientation quaternion	SST_PSO	PRM	(-)	1	E/I
Satellite attitude quaternion	EGG_NOM	IAQ	(-)	1	B/I
Angular rate	EGG_NOM	GAR	rad/s	1	B
Angular acceleration	EGG_NOM	CGA	rad/s ²	1	B
Magnetometer	AUX_NOM	MGM[1/2/3]_[X/Y/Z]_out ^a	nT	1/16	S
Magnetic torquer current	MTR_POFF ^b	(-)	A	1	S
Ion engine current	AUX_NOM	MAGNET_CURRENT_8	mA	1/8	(-)
Ion engine commanded thrust	AUX_NOM	THRUST_DEMAND_8	μ N	1/8	S
Latch valve setting	AUX_NOM	GCDE_[A/B]_LV[1/2/3/4] ^a	(-)	1/16	(-)
Inertia, center of mass	Mass property file ^c	(-)	kgm ² ,m	weekly	(-)
Solar panel currents	Personal communication ^b	PCU[1/.../6]_INPUT_CUR ^a	A	1/16	(-)

^a Different field names are indicated by options in square brackets.

^b This data was provided by ESA separately upon request, as the related fields are not available in AUX_NOM or incorrectly converted from binary data.

^c Available at `earth.esa.int/goce`.

between 0 and 180 degrees over the Northern hemisphere, and close to 90 and 270 degrees over the North and South pole respectively.

All instrument data has been (re)sampled using linear interpolation at 0.1 Hz before further processing. Only the magnetometer data is provided at a lower rate than this. As the magnetic field varies smoothly over the orbit, the upsampling by interpolation of this data will not invalidate the presented results.

3. Torque models

The main result of this work is a toolbox containing models for each significant torque acting on the GOCE satellite. The total modeled torque (indicated with a bar) can be described as a sum of individual contributions

$$\bar{\mathbf{T}} = \bar{\mathbf{T}}_M + \bar{\mathbf{T}}_A + \bar{\mathbf{T}}_G + \bar{\mathbf{T}}_S + \bar{\mathbf{T}}_I, \quad (1)$$

where $\bar{\mathbf{T}}_M = \bar{\mathbf{T}}_T + \bar{\mathbf{T}}_{D,I} + \bar{\mathbf{T}}_D$ is the total magnetic torque, caused by the magnetic control torquers ($\bar{\mathbf{T}}_T$), the ion thruster's main magnet ($\bar{\mathbf{T}}_{D,I}$), and other magnetic parts of the satellite bus and payload ($\bar{\mathbf{T}}_D$). In this paper the latter is split into a component known a-priori that is mostly due to the spacecraft bus ($\bar{\mathbf{T}}_{D,B}$), and a component that had to be estimated and stems primarily from the payload ($\bar{\mathbf{T}}_{D,P}$). $\bar{\mathbf{T}}_A$ is the aerodynamic torque, $\bar{\mathbf{T}}_G$ the gravity gradient torque, $\bar{\mathbf{T}}_S$ signifies the torque caused by solar radiation pressure and Earth albedo, and finally $\bar{\mathbf{T}}_I$ is the torque caused by misalignment of the ion thruster with respect to the satellite center of mass. In this section, each of these models is described. In relevant cases the sensitivity of the models to existing uncertainties is also analyzed. All modeled torques are plotted in Fig. 2 for a representative orbit on May 28, 2011, to provide an overview of their individual magnitude and trend.

3.1. Magnetic control

To control the attitude, GOCE had three magnetic torquers, nominally aligned with the body principal axes. To accommodate the torquers, magnetometers were installed to measure the Earth magnetic field.

A magnetic torquer induces a torque by creating a magnetic dipole $\boldsymbol{\mu}_T$. The dipole has a natural tendency to orient itself along the local magnetic field lines, which are assumed to be equal to the local Earth magnetic field lines \mathbf{B}_E . This results in a torque

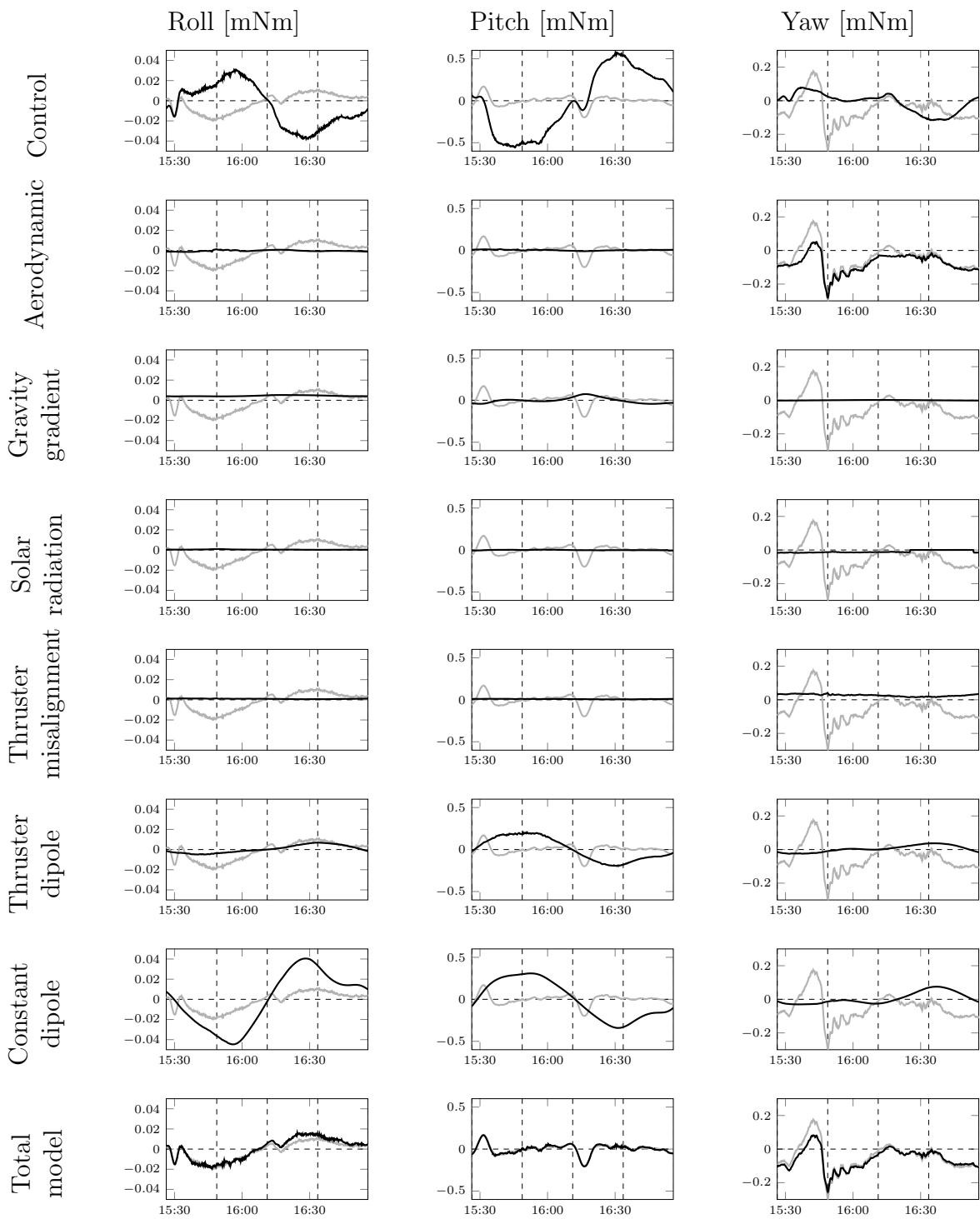


Figure 2: The output from all individual models (black) for a representative orbit on May 28, 2011, compared to the total measured torque (gray). The plot starts and ends at the ascending nodes, passing through the Northernmost point, descending node, and Southernmost point of the orbit, in that order, indicated with dashed vertical lines.

$$\bar{\mathbf{T}}_T = \boldsymbol{\mu}_T \times \mathbf{B}_E. \quad (2)$$

The dipole is directly related to the current running through the device. This dependence can be modeled as an adaptive cubic relation (Cometto, 2007).

Because the magnetometers of GOCE were situated inside the satellite body, their readings require thorough calibration. During pre-launch testing it was found that the main contributors to measurement errors were a constant internal dipole and the magnetic torquer activation (Kolkmeier et al., 2008). Therefore a calibration is performed that accounts for both these elements, alongside a bias \mathbf{B}_B and scale factor S_E . That is, we assume the magnetometer readings \mathbf{B}_M are given by

$$\mathbf{B}_M = S_E \mathbf{B}_E + (\mathbf{A}_C \boldsymbol{\mu}_C + \mathbf{B}_B) + \mathbf{A}_T \boldsymbol{\mu}_T, \quad (3)$$

where $\mathbf{A}_C \boldsymbol{\mu}_C$ and $\mathbf{A}_T \boldsymbol{\mu}_T$ are the magnetic field due to a constant on-board dipole and the magnetic torquer activation, respectively. Note that Eq. (3) is linear in the torquer dipole $\boldsymbol{\mu}_T$, as is the magnetic field it causes. Instead of modeling the magnetic field caused by the torquers at the magnetometer location, this relation is estimated and collected in the matrix \mathbf{A}_T . Note also that the constant terms due to the constant dipole $\boldsymbol{\mu}_C$ and the magnetometer bias (in brackets in Eq. (3)) can not be estimated separately based on in-orbit measurements.

By performing a least squares fit in which \mathbf{B}_E is replaced by the IGRF model output, the three magnetometers are calibrated individually. The parameters are estimated for each day of the mission. A linear fit is estimated that describes every parameter as a linear drift in time from a starting value. On four occasions during the mission the back-up GPS receiver is switched on, resulting in a different on-board dipole. As this directly affects the magnetometer bias, these episodes are treated separately from the rest of the mission for that calibration parameter. The switches are also observed in some of the scale factors. These jumps in scale factors are however considered too small relative to the nominal scale factor variation to be taken into account. The result of the calibration procedure is shown in Fig. 3 for one of the magnetometers. The magnetic torquer factors show a yearly oscillation around the linear trend. As the amplitude of this error increases over the mission, it is likely linked to the larger torquer activation later in the mission. As the magnetic disturbance is linearly related to the magnetic dipole of the torquers, this non-linearity is considered a calibration error.

The calibration matrices for each magnetometer are obtained from the linear relations. Then the calibrated signals from each magnetometer are combined into one measurement in each direction by a weighted sum, with the inverse of the remaining root mean square error (RMSE, taken over one full month) between the signal and the IGRF as weights.

In the plots of the control torque $\bar{\mathbf{T}}_T$ in Fig. 2 we can distinguish what seem to be periods of strong attitude correction in pitch. These consist of smooth peaks just after passing the ascending and descending nodes, at the start and halfway through the plotted time window respectively. It is unclear whether these maneuvers are caused by external disturbances or the internal control algorithm.

An uncertainty in the range from 0% to +10% is reported for the maximum dipole of each magnetic torquer (Kolkmeier et al., 2008). As the residual shows some similarity to the control torque throughout the mission, we have assumed this uncertainty holds throughout the linear control range. This scale factor is estimated along with the payload dipoles, as described in Section 3.6.

3.2. Aerodynamics

At the low altitude of GOCE, aerodynamic effects cause the main linear disturbance, especially as drag in the direction of flight. In terms of angular disturbances, the aerodynamic effects are especially clear in yaw, where they form the main cause of torque. This is partly due to the loose control in this direction, allowing GOCE to behave like a weather vane.

To model the aerodynamic torque the standard model

$$\bar{\mathbf{T}}_A = (\mathbf{C}_{M,A} l_{ref} + (\mathbf{r}_{ref} - \mathbf{r}_{com}) \times \mathbf{C}_{F,A}) \frac{1}{2} \rho |\mathbf{v}|^2 A_{ref} \quad (4)$$

is used, where $(\mathbf{r}_{ref} - \mathbf{r}_{com})$ is the arm from the reference point in the aerodynamic model to the center of mass of the satellite, ρ is the atmospheric neutral density, and \mathbf{v} is the total flow velocity. The moment coefficients $\mathbf{C}_{M,A} = (C_l, C_m, C_n)^T$ and force coefficients $\mathbf{C}_{F,A} = (C_X, C_Y, C_Z)^T$ are obtained from a Monte-Carlo simulation in the Analysis of Non-Gravitational Accelerations due to Radiation and Aerodynamics (ANGARA) software. All coefficients are given as a function of angle of attack α_A , angle of sideslip β_A and speed ratio S in a data table. This table is interpolated linearly. Because the speed ratio differs per atmospheric constituent, the contributions are interpolated individually and weighted with their respective density ratio

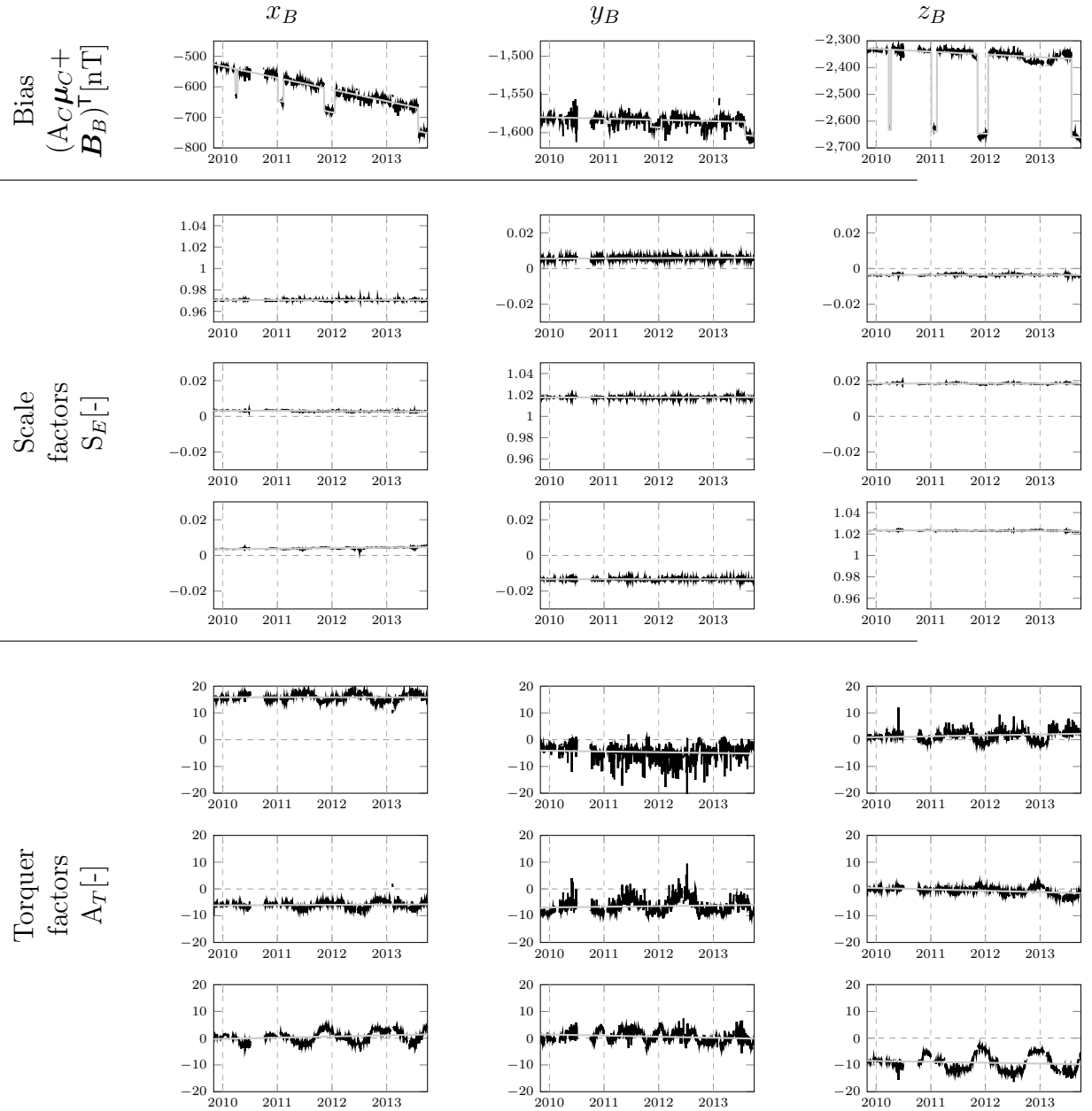


Figure 3: Daily magnetometer bias, scale factors, and magnetic torquer factors estimates (black) and the fitted linear trends (gray).

(Doornbos, 2011). Reference area A_{ref} and length l_{ref} were set to one within the ANGARA software. ANGARA provides coefficients for incoming and for outgoing particles, which are combined using the square root of the ratio of wall temperature to atmospheric temperature.

The velocity of incoming particles \mathbf{v} not only scales the torque, but it also sets the parameters used to interpolate the ANGARA coefficients. It is assumed to consist of three parts, being the orbital velocity \mathbf{v}_O , the velocity due to co-rotation of the atmosphere with the Earth \mathbf{v}_C , and thermospheric wind velocities \mathbf{v}_W . In GPS measurements however, the velocity is measured with respect to the Earth's surface, providing $\mathbf{v}_O + \mathbf{v}_C$ directly. As stated in Section 2 the wind and density measurements stem from the linear accelerations of GOCE, whereas the number densities per constituent and the local temperature are found through NRLMSISE-00.

In Fig. 2 the aerodynamic torque is plotted for one orbit. It is evident that the controller is more dominant in roll and pitch than it is in yaw. Low amplitude high frequency signals occurring near the pole crossings at 15:45 and 16:30, are observed in the control torque in roll and pitch, but in the aerodynamic torque in yaw. This implies that these signals are aerodynamic in nature, and are controlling the yaw axis, whereas they are canceled by the controller in the other directions of rotation.

Because of the change of the center of mass location due to fuel consumption, the offset between the interpolated center of mass and the ANGARA reference point needs to be taken into account. In total this causes a change in torque of less than 4%. Using the beginning-of-life or end-of-life values for \mathbf{r}_{com} results in a spread in torque of approximately 1%.

A more important uncertainty lies in the physical properties of the aerodynamic model. Currently we use a fully diffusive model with full energy accommodation. A more simple panel model provided by ThalesAlenia Space, which is described by Dumontel (2010), is evaluated for different levels of accommodation in the range 0.8 to 1, to find that the aerodynamic yaw torque is insensitive to this change within 1%. In roll and pitch the torque coefficient reduces linearly with accommodation to 87% and 84% respectively for an accommodation coefficient of 0.8. The model is therefore deemed very sensitive to this parameter, which makes it an important aspect in explaining the residual in Section 4. No specular aerodynamic model was investigated.

3.3. Gravity gradient

A difference in gravitational pull at two ends of a satellite causes a torque. In general this gravity gradient torque works to rotate the satellite such, that the longest dimension becomes vertical. In the case of GOCE this is unwanted, as the longest dimension is supposed to point in the direction of flight to minimize drag.

A simple model for this torque, assuming a spherical Earth, is well known from the literature (e.g. Wie, 2008). Less well known and used are the extensions to this model due to zonal harmonics, as presented by Roithmayr (1991). Adding only the J_2 term to the basic (spherical) expression, we obtain

$$\begin{aligned} \bar{\mathbf{T}}_G = & \frac{3\mu}{r^3} \mathbf{u}_r \times \mathbf{J} \mathbf{u}_r + \\ & \frac{\mu J_2 R_E^2}{2r^5} \left(30(\mathbf{u}_r \cdot \mathbf{u}_n)(\mathbf{u}_n \times \mathbf{J} \mathbf{u}_r + \mathbf{u}_r \times \mathbf{J} \mathbf{u}_n) + \right. \\ & \left. (15 - 105(\mathbf{u}_r \cdot \mathbf{u}_n)^2) \mathbf{u}_r \times \mathbf{J} \mathbf{u}_r + 6\mathbf{u}_n \times \mathbf{J} \mathbf{u}_n \right) \end{aligned} \quad (5)$$

where \mathbf{u}_r is the unit vector pointing from the satellite center of mass towards the Earth's center of mass and \mathbf{u}_n is the unit vector along the rotation axis of the Earth, both expressed in the body frame. \mathbf{J} is the inertia tensor, r the radial distance between GOCE and the Earth's center, μ the Earth's gravitational parameter, and R_E is the Earth radius.

The modeled gravity gradient torque only plays a significant role in the roll and pitch direction, as can be concluded from Fig. 2. In roll it causes an offset, in pitch it peaks at the occurrence of high Euler angles.

The J_2 -term results in a significant contribution to the total torque. This is especially the case for the yaw axis, in which the extra term is approximately a factor 5 larger than the spherical term. The J_3 -term (also available through Roithmayr (1991)) is at least two orders of magnitude smaller than the J_2 -term, and therefore neglected. We assume that the same holds for tesseral and sectoral contributions.

3.4. Solar radiation

Although the solar radiation causes a significant disturbance force, the resulting torque on GOCE is very small. The dusk-dawn orbit results in a constant torque about the yaw axis.

The model for solar radiation pressure torques is similar in structure to the aerodynamic model of Eq. (4), namely

$$\bar{\mathbf{T}}_S = (\mathbf{C}_{M,S} l_{ref} + (\mathbf{r}_{ref} - \mathbf{r}_{com}) \times \mathbf{C}_{F,S}) A_{ref} \frac{\Phi}{2c}, \quad (6)$$

where Φ is the solar flux at the location of GOCE and c is the speed of light. $\mathbf{C}_{M,S}$ and $\mathbf{C}_{F,S}$ are the solar radiation coefficients for forces and torques respectively, again obtained from the ANGARA software. Contrary to the aerodynamic coefficients, they only depend on the incidence angles α_S and β_S . Again, the reference area and length are set equal to one. In the validation process the roll coefficient from ANGARA was found to be wrong, and was therefore replaced by a simpler panel model (see Section 4.4). A simple model is implemented to detect and account for eclipses (Doornbos, 2011).

The Earth's infrared radiation and albedo are also taken into account, for the sake of completeness. In the model, adopted from Doornbos et al. (2009), the Earth surface is subdivided in one degree longitude by one degree latitude quadrilaterals. For all elements it is decided whether they are visible from GOCE and, for the albedo model, from the Sun. Then Lambert's law is applied to the incoming sunlight, the outgoing reflected sunlight, and the outgoing infrared radiation. The resulting fluxes are multiplied with the monthly-mean top-of-atmosphere all-sky albedo and longwave flux respectively, obtained from the CERES SYN1deg product (Edition 3A). The resulting torque is added to the direct solar radiation torque.

The model output is shown in Fig. 2 for one orbit. Solar radiation mainly causes an offset in the yaw torque when GOCE is not in eclipse.

Varying the location of the center of mass over the range of possible values results in a range of torques differing by less than 4%. Even in the most extreme case no significant contribution to the total torque is thus to be expected.

3.5. Ion thruster

To compensate for drag, GOCE is equipped with an ion thruster. When the thrust does not point directly through the center of mass, it causes a torque. Therefore the thruster is pointed such that it aims in the center of mass range. Over the course of the mission the center of mass will shift due to fuel consumption, causing a slowly changing misalignment torque.

The model for the torque due to thruster misalignment, denoted by $\bar{\mathbf{T}}_I$, is simply the cross product between the arm from the thruster position \mathbf{r}_T

to the center of mass of the satellite \mathbf{r}_{com} and the thrust vector \mathbf{F}_I .

$$\bar{\mathbf{T}}_I = (\mathbf{r}_T - \mathbf{r}_{com}) \times \mathbf{F}_I. \quad (7)$$

The thruster position and thrust direction were obtained from Cometto (2007).

The misalignment torque is plotted for one orbit in Fig. 2. The misalignment causes a significant offset in the yaw torque, but shows no great influence in the other directions. The change in altitude over the orbit causes a change in density and therefore in thruster activation, which is directly introduced into the torque (visible as a dip in Fig. 2 around 16:30).

Changing the location of the center of mass over the specified mission range does not significantly affect $\bar{\mathbf{T}}_I$. The direction of \mathbf{F}_I is a more sensitive parameter. A sensitivity analysis proved that an alignment error of 0.1° around the y_B -axis may already increase this torque by a factor of 3.5. Similar results are obtained in roll and yaw direction when rotating the torque around the z_B -axis instead. The reported error margin of 0.90° half-cone angle around the y_B -axis and 0.05° around the z_B -axis (Kolkmeier et al., 2008) therefore leaves a wide range of possible model outputs.

The ion thruster assembly includes a large electromagnet. The dipole of this magnet, $\boldsymbol{\mu}_I$, is modeled as a linear function of the current running through it (Kolkmeier et al., 2008), and a term for the product of torquer and thruster magnet current, as

$$\boldsymbol{\mu}_I = (\boldsymbol{\mu}_{I,H} + M_{I,S} \mathbf{I}_T) I_I. \quad (8)$$

Here $\boldsymbol{\mu}_{I,H}$ is the hard magnetic part induced by the electromagnet in the ion thruster, $M_{I,S}$ is a 3×3 matrix representing the soft magnetic part depending on the torquer activation, and \mathbf{I}_T and I_I are the three torquer currents and the thruster current respectively. Note that the sign of the documented dipole was found to be wrong (as discussed in Section 4.5) and therefore changed.

The thruster magnet current is filtered to remove sampling noise caused by the on-board down-sampling from 100Hz to 1/8Hz in the housekeeping data. It was observed that the most noisy periods coincide with episodes of high noise in the recorded thrust. Therefore an exponential moving average filter is used that is locally adapted with the difference between the commanded and recorded thrust. The filter, with a width of 9 data points, takes the form

$$I_I = \frac{\sum_{i=-4}^4 I_I^{\text{unfiltered}} \exp\left(\frac{-0.01|i|}{\nu}\right)}{\sum_{i=-4}^4 \exp\left(\frac{-0.01|i|}{\nu}\right)}, \quad (9)$$

where ν is the triangular mean square error between commanded and recorded thrust in the filter window.

The magnetic torque from the ion thruster is plotted separately in Fig. 2. The torque is dominated by a trend comparable to that of the constant dipoles (discussed hereafter), but a high frequency signal can be seen in pitch at locations near the magnetic poles where strong wind and density variations are expected.

3.6. Constant dipoles of spacecraft bus and payload

The magnetic dipoles of equipment on GOCE play an important role in modeling the total torque. Currently information is only available for dipoles caused by the spacecraft bus. The magnetic dipoles caused by the payload have to be estimated.

The constant bus dipoles can be subdivided in two categories. The first are due to long term, hard magnetic effects $\boldsymbol{\mu}_{B,H}$ in the fuel tanks and latch valves. These cause the main part of the total magnetic torque on the spacecraft. When electric components of the bus, such as valves, are switched on or off, the hard magnetic dipole can suddenly change. During nominal operations no such events were observed. Soft magnetic dipoles form the second category. Contrary to hard magnetic effects, these dipoles are induced by a local magnetic field. In this case the dipole is assumed to depend linearly on the local Earth's magnetic field strength (through matrix $M_{B,S}$) and the torquer currents (through $M_{B,T}$). Combined these contributions result in a magnetic torque (Kolkmeier et al., 2008)

$$\bar{\boldsymbol{T}}_{D,B} = (\boldsymbol{\mu}_{B,H} + (M_{B,S} + M_{B,T}|\boldsymbol{I}_T|)\boldsymbol{B}_E) \times \boldsymbol{B}_E, \quad (10)$$

with $|\boldsymbol{I}_T|$ the L^2 -norm of the currents to the magnetic torquers, and \boldsymbol{B}_E the Earth's magnetic field obtained from the calibrated magnetometer measurements.

The magnetic torque $\bar{\boldsymbol{T}}_{D,B}$ only includes magnetic effects from the spacecraft bus. For the dipoles of the payload (gradiometer and GPS system), no data is available. Calculating the residual torque as described in the next

section, it is found that these missing magnetic dipoles have a significant influence on the model quality. In the remainder of this section the procedure to estimate the dipoles is described, as well as the model result.

First of all the residual, unmodeled torque is obtained by reducing the measured torque by all model outputs described before. The result reveals a periodic signal that repeats every 10.5 minutes ($1.59 \times 10^{-3} \text{Hz}$). This is not a higher mode of the orbital frequency or a contribution from any of the models, and is therefore considered an artifact of the data processing. As the signal is most prominent in the roll and pitch axes, and it was to our knowledge not observed in the linear accelerations before, this signal most likely stems from the attitude determination and control system. The signal is removed from the residual by a series of seven notch filters centered at the central frequency and the closest two lower and four higher modes.

Second of all it must be decided what types of dipoles are to be fitted. From the earlier discussion it is clear that we can distinguish between constant and variable dipoles on one hand, and hard magnetic and soft magnetic dipoles on the other. To prevent fitting to the control algorithm or aerodynamic signals, no variable dipoles are estimated. The constant hard magnetic dipole $\boldsymbol{\mu}_{P,H}$ is simply a three element vector, whereas the soft magnetic dipole is assumed to be linearly dependent on the Earth magnetic field through a 3×3 -matrix $M_{P,S}$. As discussed in Section 3.1 a full 3×3 scale matrix S_T for the control dipoles is estimated alongside above mentioned dipoles. To prevent overfitting to for example a remaining bias in the measured torque, or an error in the aerodynamic model, a three element offset vector \mathbf{T}_{off} is estimated alongside the dipoles. Combining the above contributions, we assume that the measured torque can be written as

$$\begin{aligned} \mathbf{T} &= \bar{\mathbf{T}} + \bar{\mathbf{T}}_{D,P} + \mathbf{T}_{off} + \boldsymbol{\varepsilon} \\ &= \bar{\mathbf{T}} + (\boldsymbol{\mu}_{P,H} + M_{P,S} \mathbf{B}_E + S_T \boldsymbol{\mu}_T) \times \mathbf{B}_E + \mathbf{T}_{off} + \boldsymbol{\varepsilon}, \end{aligned} \quad (11)$$

with $\boldsymbol{\varepsilon}$ a random error. Note that contrary to the definition of $\bar{\mathbf{T}}$ in Eq. (1) we exclude $\bar{\mathbf{T}}_{D,P}$ from the total model here and explicitly add it as a term in the equations.

Third of all the elements of $\boldsymbol{\mu}_{P,H}$, $M_{P,S}$, S_T , and \mathbf{T}_{off} are estimated by minimizing the weighted square error

$$\min \quad \boldsymbol{\varepsilon}^\top \mathbf{W}^2 \boldsymbol{\varepsilon}, \quad (12)$$

where the diagonal weight matrix W is constructed using a local central estimation scheme. In this scheme Eq. (12) is solved using ordinary least squares at each time instant, based on the closest 47 data points (23 both forward and backward in time). The local weight is then defined as the inverse of the root mean square error between the local fit and the residual torque over the full range of 47 data points.

To solve the minimization problem in Eq. (12) the estimated torque in Eq. (11) is rewritten to

$$\bar{\mathbf{T}}_{D,P} = -\mathbf{B}_{E,H}\boldsymbol{\mu}_{P,H} - \mathbf{B}_{E,S}\mathbf{M}_{P,S} - \mathbf{B}_{E,T}\mathbf{S}_T, \quad (13)$$

where $\mathbf{B}_{E,H}$ is the cross-product matrix with the elements of \mathbf{B}_E . The vector $\mathbf{M}_{P,S}$ is the vectorization of $\mathbf{M}_{P,S}^T$, and the 3×9 -matrix $\mathbf{B}_{E,S}$ is defined as

$$\mathbf{B}_{E,S} = \begin{bmatrix} \mathbf{0} & -\mathbf{B}_E^T B_{E,z} & \mathbf{B}_E^T B_{E,y} \\ \mathbf{B}_E^T B_{E,z} & \mathbf{0} & -\mathbf{B}_E^T B_{E,x} \\ -\mathbf{B}_E^T B_{E,y} & \mathbf{B}_E^T B_{E,x} & \mathbf{0} \end{bmatrix}. \quad (14)$$

Similarly, \mathbf{S}_T is the vectorization of \mathbf{S}_T^T and the 3×9 -matrix $\mathbf{B}_{E,T}$ is obtained from Eq. (14) by replacing all occurrences of the magnetic field vector \mathbf{B}_E^T by the torquer dipole $\boldsymbol{\mu}_T^T$.

By collecting $\boldsymbol{\mu}_{P,H}$, $\mathbf{M}_{P,S}$, and \mathbf{S}_T in a single column vector, and combining the matrices accordingly, the dipoles and scale factors can be fitted simultaneously. The offset \mathbf{T}_{off} is included in the estimation by adding a 3×3 identity matrix \mathbf{I}_3 . Setting $\bar{\mathbf{T}}_{D,P} = \mathbf{T} - \bar{\mathbf{T}}$, filling in $\mathbf{B}_E = [-\mathbf{B}_{E,H}, -\mathbf{B}_{E,S}, -\mathbf{B}_{E,T}, \mathbf{I}_3]$, and collecting these over the measurements 1 up to n , we may solve for the dipole estimate (indicated with a hat) as

$$\begin{pmatrix} \hat{\boldsymbol{\mu}}_{P,H} \\ \hat{\mathbf{M}}_{P,S} \\ \hat{\mathbf{M}}_T \\ \hat{\mathbf{T}}_{off} \end{pmatrix} = \left(\mathbf{W} \begin{bmatrix} (\mathbf{B}_E)_1 \\ \vdots \\ (\mathbf{B}_E)_n \end{bmatrix} \right)^+ \mathbf{W} \begin{pmatrix} (\mathbf{T} - \bar{\mathbf{T}})_1 \\ \vdots \\ (\mathbf{T} - \bar{\mathbf{T}})_n \end{pmatrix}. \quad (15)$$

The cross product in Eq. (11) is not invertible due to the soft magnetic part $\mathbf{M}_{P,S}$. This is best illustrated by writing the dipole matrix as $\mathbf{M}_{P,S} = \mathbf{M} + m\mathbf{I}_3$. Filling this into Eq. (11) and writing out the cross product, we find the term $m\mathbf{I}_3\mathbf{B}_E \times \mathbf{B}_E$, which is zero, independent of m . This diagonal value is thus arbitrary, leaving one degree of freedom unresolved. Therefore the Moore-Penrose pseudo-inverse ($^+$) is used.

Daily estimates of the payload dipoles are computed for the whole mission (see Fig. 4). A linear fit is made for each element, to allow for ageing of satellite components. For the hard magnetic dipole $\hat{\boldsymbol{\mu}}_{P,H}$ two separate linear fits are made, one for when the redundant GPS receiver is off (the nominal case), and one for when it is turned on (the highlighted periods in the top row of Fig. 4)). It is assumed that the other dipole elements are not affected by this receiver. The parameters of the linear trends can be found in Table 4.

Finally the estimated torque becomes

$$\hat{\boldsymbol{T}}_{D,P} = \left(\hat{\boldsymbol{\mu}}_{P,H} + \hat{M}_{P,S} \boldsymbol{B}_E + \hat{S}_T \boldsymbol{\mu}_T \right) \times \boldsymbol{B}_E. \quad (16)$$

In Fig. 2 the constant bus and payload dipole torques are plotted together. The constant magnetic dipoles cause the largest disturbance torques in roll and pitch, and with that dictate the low frequency trend in the control torque.

It is unclear up to what extent the reported bus dipoles are correct. For some contributions an indeterministic part is given in the documentation, which in a few cases implies an error margin of 10% (Kolkmeier et al., 2008). Most of these errors are expected to be eliminated by the estimation of the payload dipoles.

4. Validation

Combining the models of Section 3 we find a total modeled torque $\bar{\boldsymbol{T}}$. To compare this to the measurements, the measured angular acceleration is combined with the angular rate to find a measured torque \boldsymbol{T} . This is done using the well-known relation

$$\boldsymbol{T} = \boldsymbol{J}\boldsymbol{\alpha} + \boldsymbol{\omega} \times \boldsymbol{J}\boldsymbol{\omega}. \quad (17)$$

Here \boldsymbol{J} is the interpolated inertia tensor, $\boldsymbol{\alpha}$ is the measured angular acceleration, and $\boldsymbol{\omega}$ is the measured angular rate of the satellite body.

The angular acceleration product EGG_CGA is not fully calibrated. A bias from the expected zero-mean can be observed, that drifts over the mission. Therefore a calibration effort was performed similar to the one described for the magnetometers in Section 3.1. In this case the mean angular acceleration was calculated for each day. Then a cubic polynomial was estimated to catch the drifting trend. The resulting bias is shown in Fig. 5. Note that the accelerometers were calibrated regularly during the mission, causing the

Table 4: Parameters of the linear fits of the daily dipole estimates. Time t is expressed in days since the start of the science phase of the mission (November 1, 2009).

Dipole	x_B	y_B	z_B
Hard dipole $\hat{\boldsymbol{\mu}}_{P,H}^\top$ (SSTI-B off) [Am^2]	$-0.85 + 5.11 \times 10^{-5}t$	$0.70 - 5.46 \times 10^{-5}t$	$-1.68 + 1.36 \times 10^{-4}t$
Hard dipole $\hat{\boldsymbol{\mu}}_{P,H}^\top$ (SSTI-B on) [Am^2]	$-0.89 + 2.29 \times 10^{-4}t$	$0.83 - 1.39 \times 10^{-4}t$	$-1.69 + 2.27 \times 10^{-4}t$
Soft dipole $\hat{M}_{P,S}$ [mAm^2/nT]	$-0.0155 + 1.80 \times 10^{-6}t$	$0.0006 + 8.39 \times 10^{-6}t$	$-0.0011 + 3.63 \times 10^{-6}t$
	$0.0096 - 2.22 \times 10^{-7}t$	$0.0154 - 1.81 \times 10^{-6}t$	$-0.0058 + 1.88 \times 10^{-7}t$
	$0.0047 - 5.52 \times 10^{-7}t$	$-0.0009 + 1.49 \times 10^{-6}t$	$0.0001 + 6.15 \times 10^{-9}t$
	$0.0844 - 1.05 \times 10^{-5}t$	$-0.0197 + 2.65 \times 10^{-5}t$	$0.0105 + 4.39 \times 10^{-6}t$
Torquer scale factors \hat{S}_T [-]	$0.0105 - 3.55 \times 10^{-7}t$	$0.0755 - 1.36 \times 10^{-5}t$	$0.0036 + 1.73 \times 10^{-6}t$
	$0.0005 - 5.38 \times 10^{-6}t$	$-0.0209 + 2.51 \times 10^{-5}t$	$0.0555 - 4.16 \times 10^{-6}t$
Offset $\hat{\boldsymbol{T}}_{off}^\top$ [mNm]	$-848.2 + 5.11 \times 10^{-2}t$	$701.8 - 5.46 \times 10^{-2}t$	$-1679.9 + 1.36 \times 10^{-1}t$

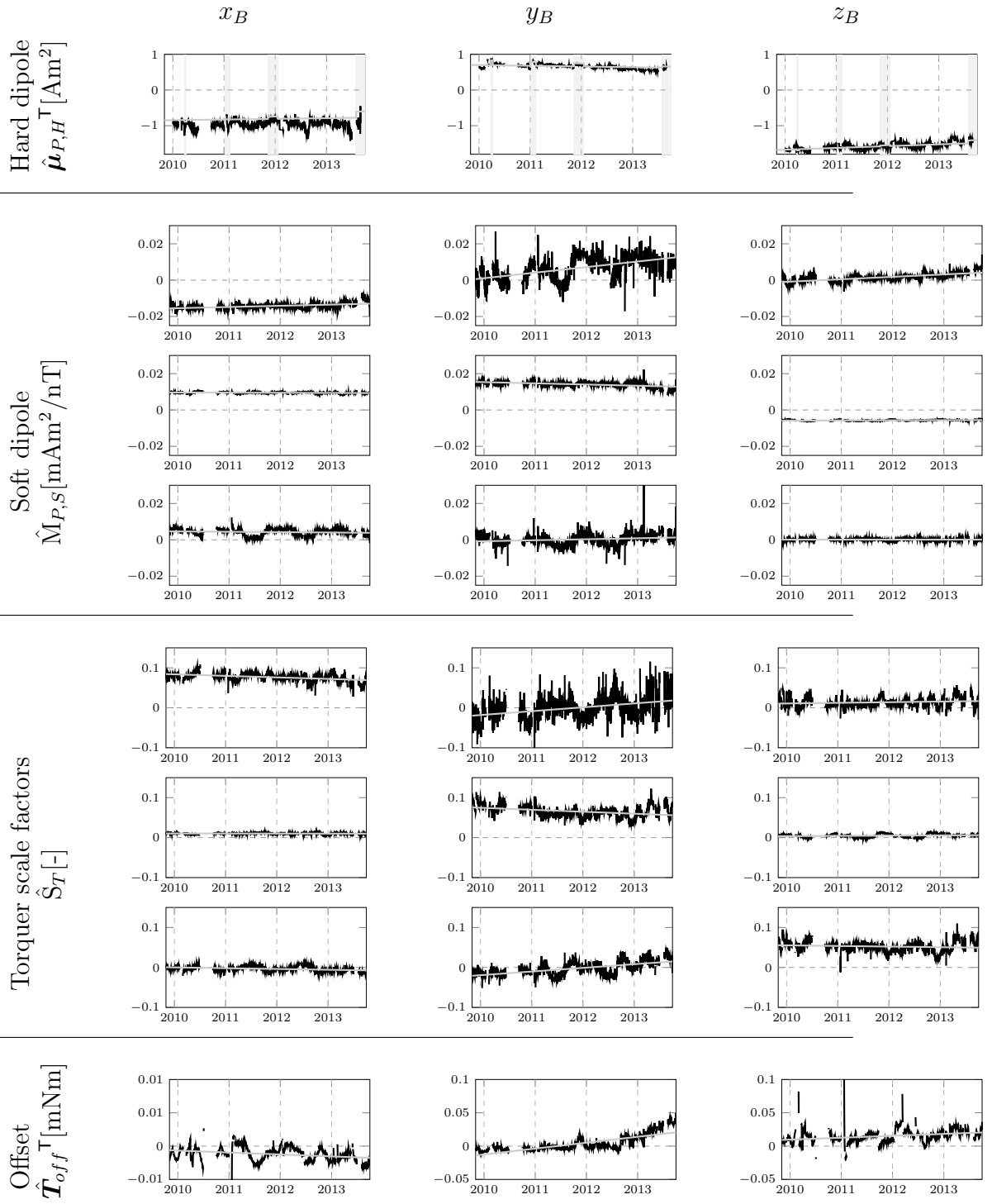


Figure 4: The daily estimates of payload dipoles, torquer scale factors, and torque offsets over the entire mission, with the linear fits in gray. In the top row the episodes when the redundant GPS system was turned on are highlighted in light gray.

need for several cubic fits over parts of the mission. The bias in pitch acceleration was very small overall. To prevent overfitting to the noise in the daily means, linear fits were made for this component.

By taking the difference between the measured torque \mathbf{T} (plotted for May 19 to 31, 2011 in Fig. 6) and the total modeled torque $\bar{\mathbf{T}}$ (where $\bar{\mathbf{T}}_{D,P}$ is replaced by the estimate $\hat{\mathbf{T}}_{D,P}$, plotted in Fig. 7) the quality of the models can be evaluated. For May 19 to 31, 2011, this residual torque is plotted in Fig. 8. In the remainder of this section several individual torque models are validated by investigating the residual torque during special events.

4.1. Magnetic control torque

Throughout the mission the torquer activation is regularly enhanced significantly by a periodic signal in the frequency range above 15 times per orbit. A similar oscillation was observed before in the magnetic torquer activity on GRACE by Bandikova et al. (2012), but the exact cause of this behavior remains unknown. On GOCE it occurs approximately once or twice each month and lasts from a few hours to several day. The activity is clearly present in the measured pitch signal, as in Fig. 6b from May 21 to 25. Such activity allows for validating the torquer model and the estimated torquer scale factors \hat{S}_T , as it temporarily raises the control torque above the error level of other models over a fixed frequency range.

The episode under consideration here is a particularly short one, lasting only a few hours on May 5, 2011. All torques are filtered using a third-order high-pass Butterworth filter with a cut-off frequency corresponding to 15 times per orbit. The filtered residual torque $\mathbf{T} - \bar{\mathbf{T}}$ is then compared to the filtered control torque $\bar{\mathbf{T}}_T$ by calculating Pearson’s correlation coefficient. This coefficient is expected to increase if the increased torquer activation also affects the residual, i.e. the coefficient should respond only if the torquer model is incorrect. A time series is constructed by calculating the correlation coefficient over a moving central window of one orbital period. This procedure is repeated for the comparison of the residual torque before and after including the estimated torquer scale factors \hat{S}_T on the one hand, and the (documented) control torque on the other hand. The result is shown as a time series of the correlation coefficients in Fig. 9. First of all, the correlation between measured torque and modeled control torque (dashed black line) shows the importance of the control torque in the frequency range of interest. Only in yaw the correlation deviates significantly from one, indicating again the reliance on GOCE’s passive aerodynamic stability in that axis.

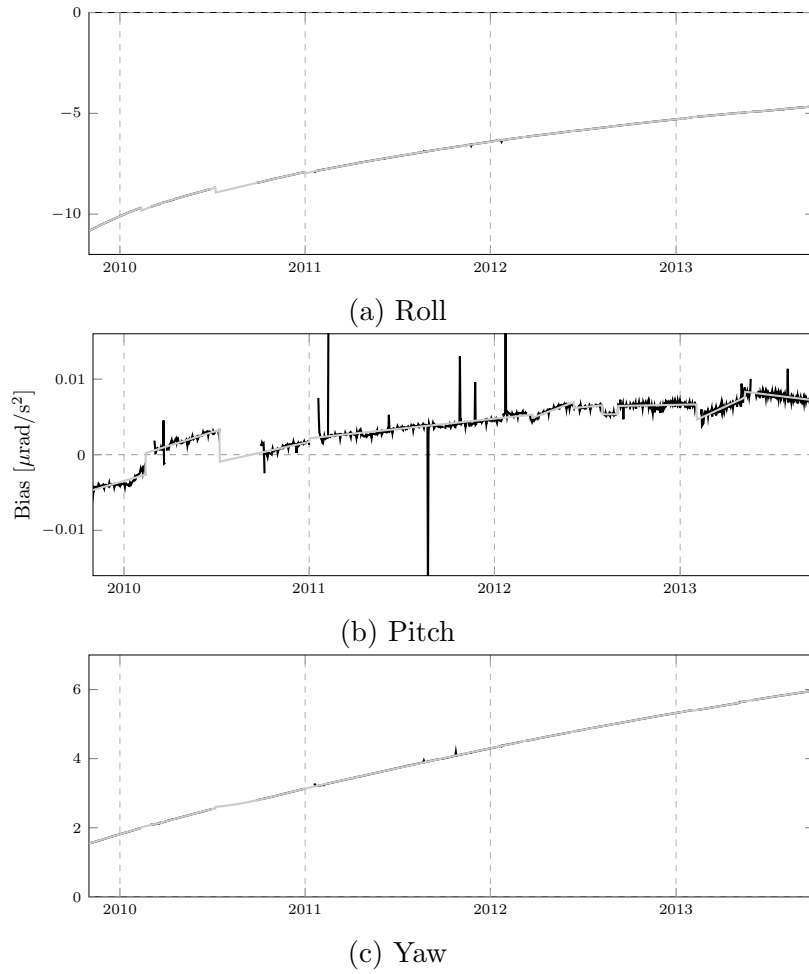


Figure 5: Bias of the three angular accelerations for the full mission, with the fitted polynomials in gray.

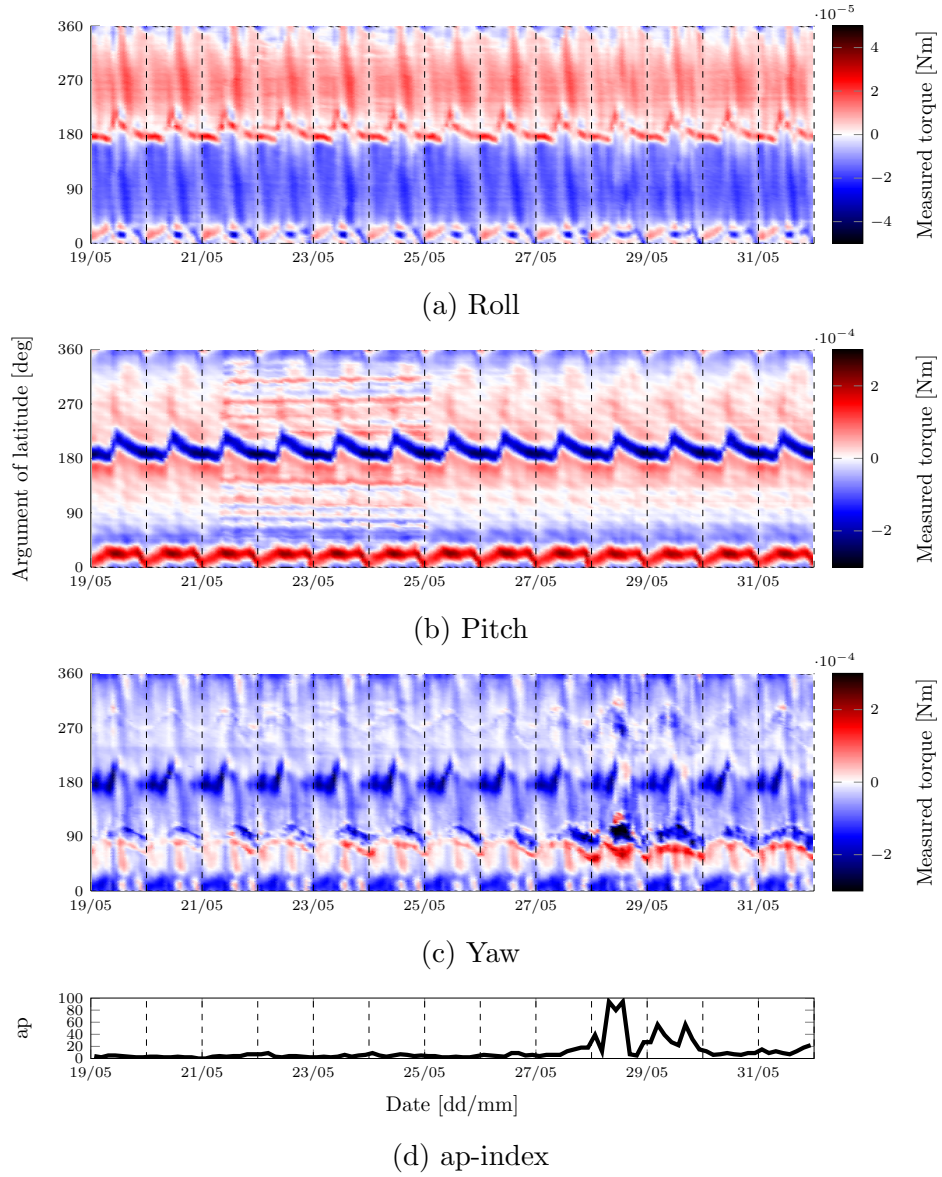


Figure 6: Measured torque between May 19 and 31, 2011.

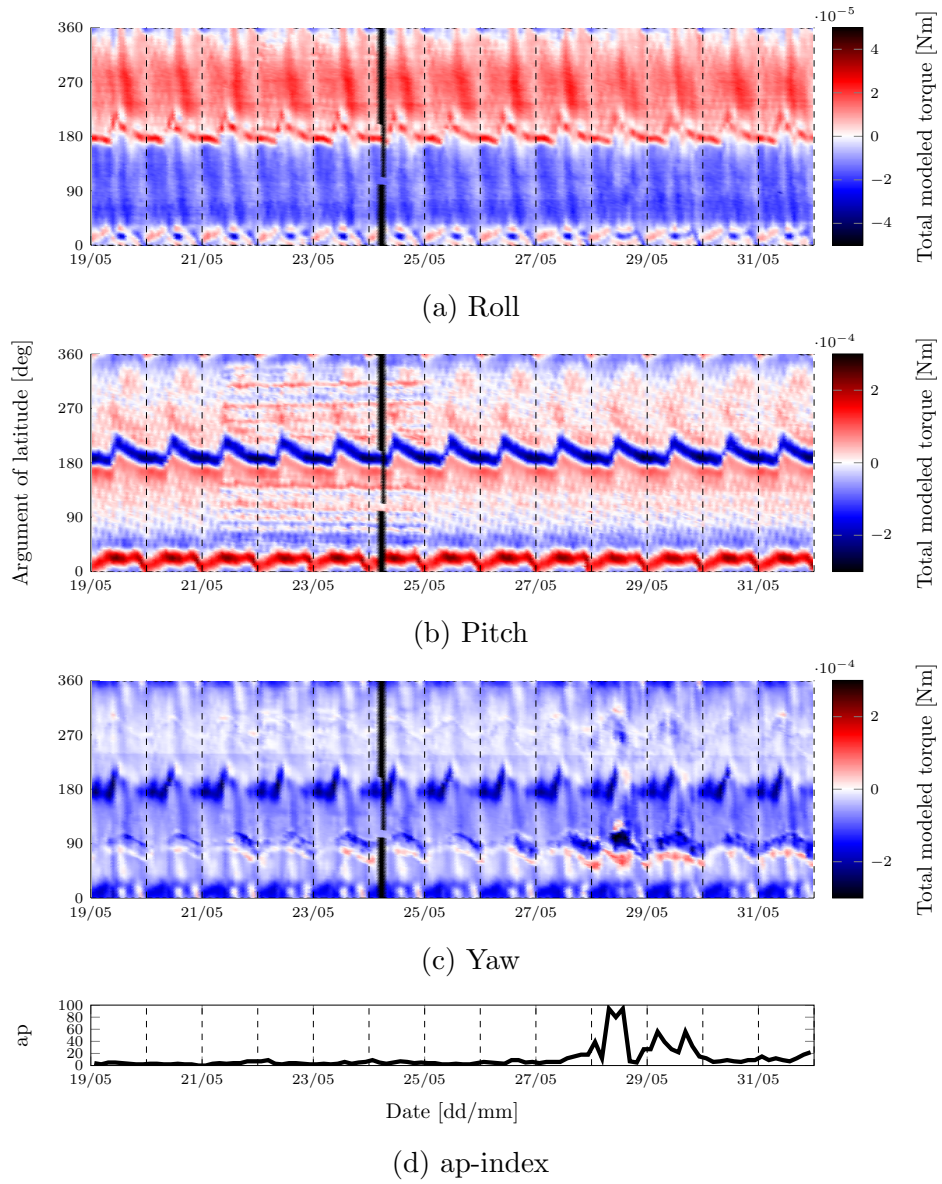


Figure 7: Total modeled torque between May 19 and 31, 2011, including estimated magnetic contributions.

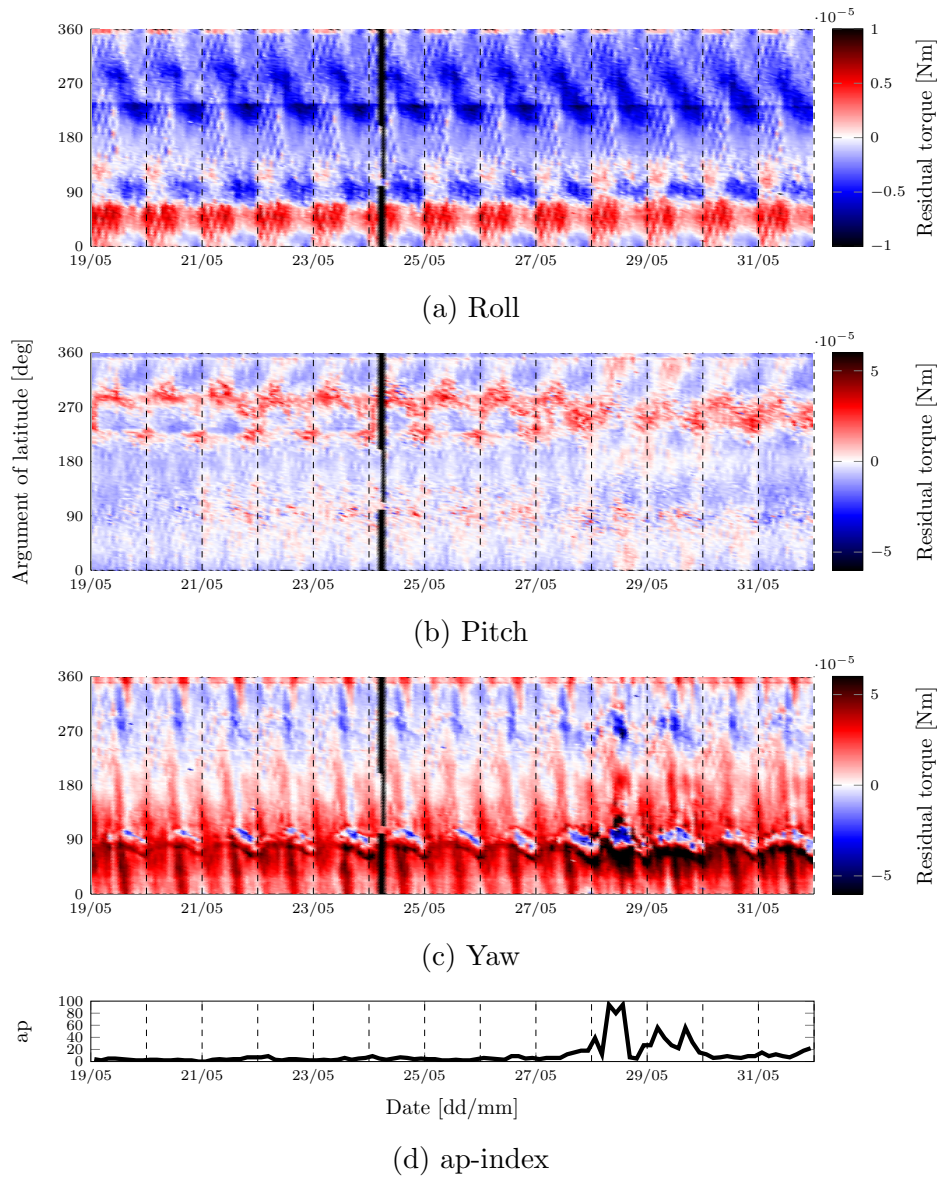


Figure 8: Residual torque between May 19 and 31, 2011, including estimated magnetic contributions. (Note different scale than 6.)

Over the highlighted episode of increased control (light gray box) the correlation between measured and control torque in pitch approaches one, while roll and yaw show no such response. The correlation between the control and the residual (solid black line) in pitch increases significantly. The inclusion of the estimated scale factors (7.5% on the x_B -directed torquer, 6.5% on y_B , and 4.8% on z_B ; up to 1.5% off-diagonal) greatly reduces this response.

In Fig. 4 the scale factor matrix elements are plotted over the full mission. The elements are approximated well by a linear trend, except for the off-diagonal elements pertaining to the y_B -directed torquer (in the second column). This torquer mostly controls the roll motion. The small scale of the torques in this direction may be the cause of this erratic behavior.

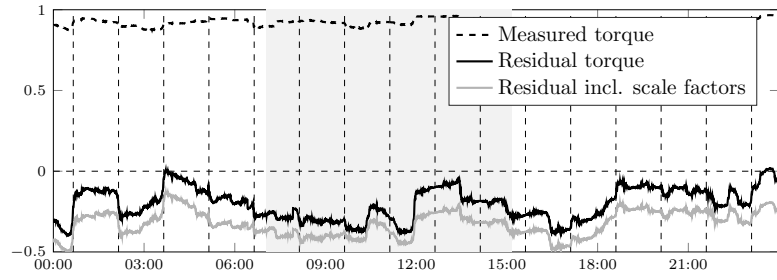
To test whether the torquer scale factors are within the documented error bounds, the 3×3 matrix must be converted to one scale factor per torquer, and a misalignment angle. Writing the total control torque as

$$\bar{\mathbf{T}}_T = (\mathbf{I}_3 + \hat{\mathbf{S}}_T)\boldsymbol{\mu}_T \times \mathbf{B}_E \quad (18)$$

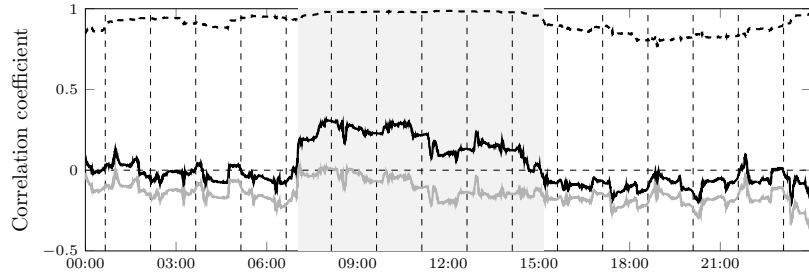
we observe that the matrix $(\mathbf{I}_3 + \hat{\mathbf{S}}_T)$ describes a scaling and rotation of the control dipole $\boldsymbol{\mu}_T$ from the three magnetic torquers. The individual scale factor per magnetic torquer is then the norm of each column of this matrix. After normalizing each column, the diagonal elements represent the cosines of the misalignment angles. Following this process, we find that the estimated linear trends produce scale factors that are within the documented uncertainty bounds of 0 to +10% (Kolkmeier et al., 2008). The misalignment of the x_B - and z_B -directed torques stay within the maximum 2° half-cone angle (Kolkmeier et al., 2008) throughout the mission, while the y_B -directed torquer violates this bound starting March of 2013, to rise to 2.4° at the end of the science mission.

4.2. Aerodynamics

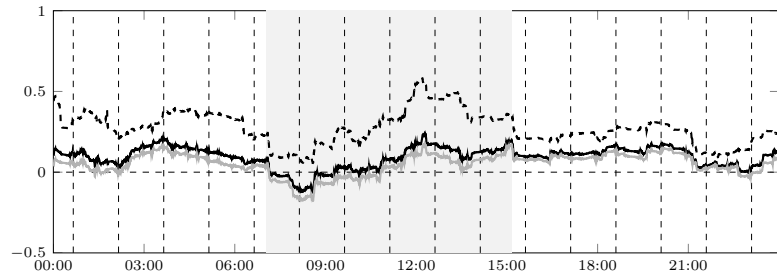
During geomagnetic storms the atmosphere is locally heated, causing it to expand. This expansion increases the neutral density in the thermosphere, as well as the wind speed at the satellite's orbital altitude. The effect on the (yaw) torque can be clearly seen in Fig. 6 on May 28. The magnetic storm of April 5, 2010 is used to validate the aerodynamic torque. The same approach is taken as for the magnetic control torque. In this case the measured and residual torque are compared to the aerodynamic model. All torques are filtered using a third-order high-pass Butterworth filter with a



(a) Roll



(b) Pitch



(c) Yaw

Figure 9: Correlation coefficients between high-pass filtered control torque on one hand, and the filtered measured torque, residual, or residual including torquer scale factors on the other hand for May 5, 2011. The highlight indicates the time of increased torquer activation.

cut-off frequency at 1.5 times per orbit, as the aerodynamic model is most active at frequencies twice per orbit and higher.

The correlation coefficients are plotted over five days surrounding the storm in Fig. 10. While the roll and pitch torques are mostly unaffected, the yaw torque residual clearly responds to the storm. The correlation between the residual and the aerodynamic model increases significantly at the start of the storm and takes on a more constant trend. The dip in correlation that occurs at the start of each day is almost entirely removed from the signal. The increased correlation between the residual and aerodynamic torque during the storm implies that the aerodynamic model represents the trend well, but fails to properly model the magnitude of the actual aerodynamic torque. Therefore we conclude that significant errors remain in the magnitudes of either the aerodynamic model coefficients or the thermospheric wind and density data.

4.3. Gravity gradient

During its mission, GOCE has not made any extreme attitude maneuvers while in science mode, making it impossible to isolate a moment in time in which the gravity gradient is the major cause of a change in torque. Therefore the residual torque is compared for different orders of the gravity model in the frequency domain. In Fig. 11 the comparison is shown for the cases with and without the J_2 -term. From this comparison it was found that, as expected, the oblateness term is an important and non-negligible contribution to the total torque. In pitch this element introduces a significant peak in the PSD of the model, that reduces the peak in the residual at twice-per-orbit frequencies. In yaw its contribution is even a factor 5 larger than that of the basic spherical Earth model. This signifies the importance of the gravity gradient torque, but due to the lack of special maneuvers no further validation can be performed.

4.4. Solar radiation pressure

Implementing the ANGARA model for all moment coefficients, it was found that the residual torque in roll strongly resembled the solar radiation pressure torque. Therefore the ANGARA coefficients were compared to a simplified fully specular 36-panel model (from Dumontel (2010), excluding the radiator). Assuming a reflectance of 0 for the solar panel-covered side and a reflectance of 0.8 for the radiator side, a close fit is found between the two models for all force and torque coefficients but the roll coefficient.

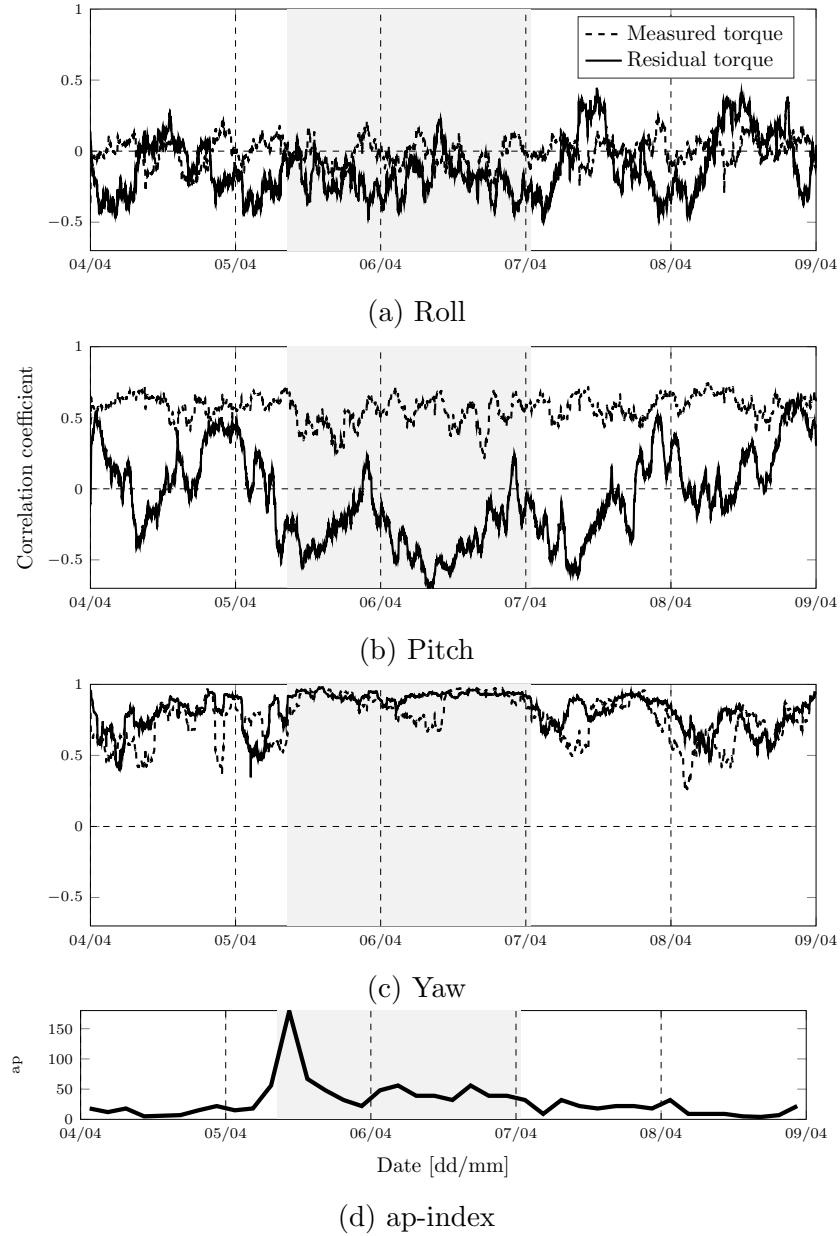


Figure 10: Correlation coefficients between high-pass filtered aerodynamic torque on one hand, and the filtered measured or residual torque on the other hand for five days in April 2010. The highlight indicates the time of increased ap-index values.

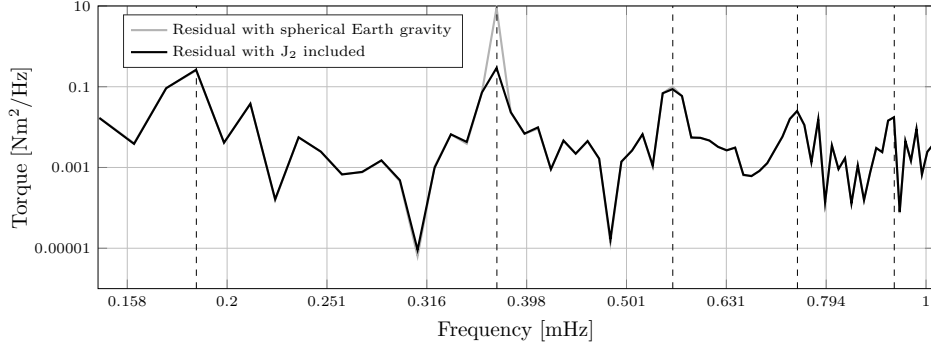


Figure 11: Frequency domain plot of the pitch torque residual when assuming gravity points radially down compared to the residual including the J_2 -term. Dashed lines indicate one up to five times the orbit frequencies.

It was therefore decided to use the several orders of magnitude smaller roll coefficient from the simplified model instead of the one obtained from the ANGARA software.

The eclipse transitions present an opportunity to validate the solar radiation pressure model using a superposed epoch analysis. In Fig. 12 the residual torque (including the solar radiation pressure) is presented for April 12 to 22, 2011, for 300 seconds before and 500 seconds after the start of the (modeled) transitions out of eclipse. During the displayed period the eclipses grow longer, from partial eclipses at the start to full eclipses of 10 minutes at the end.

The residual shows two striking trends of different nature. The first is a line of roll torque peaks running from 320 at the start of the plotted period to 120 seconds after transition at the end. The same trend can be observed as a negative pitch torque, but is not visible in the yaw direction. Because of the periodic nature of the line, showing intensity and direction fluctuations on a daily basis, it is hypothesized that this is a magnetic signal. In Fig. 13 the residual roll torque is plotted alongside the magnetometer measurements and solar panel currents for a single transition out of eclipse. As the solar panel current increases, so does the on-board magnetic field that is registered by the magnetometers. It is possible that the satellite switches from battery to solar power just after the panels reach their maximum current, about 110 seconds after the start of the transition. A magnetic dipole caused by the rapid change in current flow through the satellite could explain the steep

drop in both the on-board magnetic field and the roll torque. Attempts to estimate the dipole of the solar panels as a function of provided current did however not yield consistent results.

The second trend is a wider band of increased residual yaw torque, visible as a bright red horizontal band in Fig. 12c. It runs just below the magnetic line described above, and spans approximately 100 to 150 seconds per orbit. Because of its location, closer to the start of the transition, it is expected that this is a product of the overly simplistic eclipse model. In Fig. 14 a single transition is isolated, and the residual yaw torque is plotted against the time into transition to test this hypothesis. The eclipse transition in the solar radiation pressure model (dashed line) is clearly a factor two to three faster than the actual transition visible in the residual torque excluding the solar radiation pressure model ($\mathbf{T} - (\bar{\mathbf{T}} - \bar{\mathbf{T}}_S)$, solid gray line). This mismatch is causing the residual (solid black line) to first rapidly increase as the model transitions, and then recover to a level close to zero as the actual eclipse transition takes place. The solar radiation pressure model as a whole thus correctly represents the magnitude of the radiation torque, but fails to properly portray the eclipse transition process. Because of the overall small significance of this torque, the simplistic transition model is kept. The roll and pitch radiation torque are too small to repeat this test for those axes.

4.5. Ion thruster

In August 2012 GOCE’s orbit was lowered by deducting a constant bias from the measured acceleration before computing the required thrust. The constant acceleration was large enough to command the minimum possible thrust over part of each orbit. This month therefore provides a good opportunity to validate the thruster related torques. At the moment of adding or removing the acceleration bias, a significant change in both the residual torque and the current through the ion thruster magnet occurs. The change in thrust on the other hand is relatively small. This suggests an error exists in the thruster dipole model. Therefore a dipole with the same model structure as in Eq. (8) was estimated along with $\bar{\mathbf{T}}_{D,P}$ on each day of August 2012.

The estimated hard magnetic part $\hat{\boldsymbol{\mu}}_{I,H}$ is compared to the same element from the documented models in Kolkmeier et al. (2008) on scale and direction. The norm of the fitted dipole reduces over the month, from 99% of the documented one at the start to around 80% towards the end of August 2012. The dot product between the unit vectors remains close to -1 all through

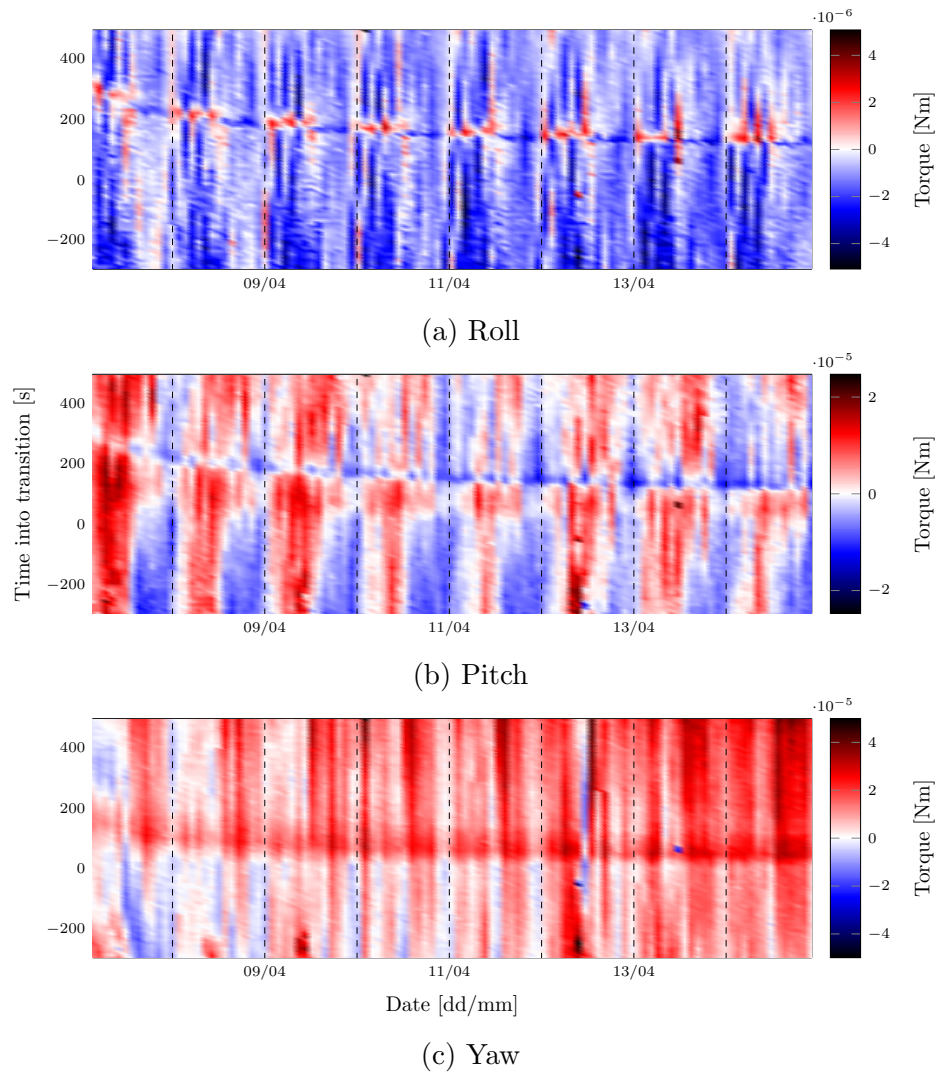


Figure 12: Residual torque during transitions out of eclipse over eight days in April 2011. The vertical axis represents the time in seconds since the start of the transition according to the solar radiation pressure model.

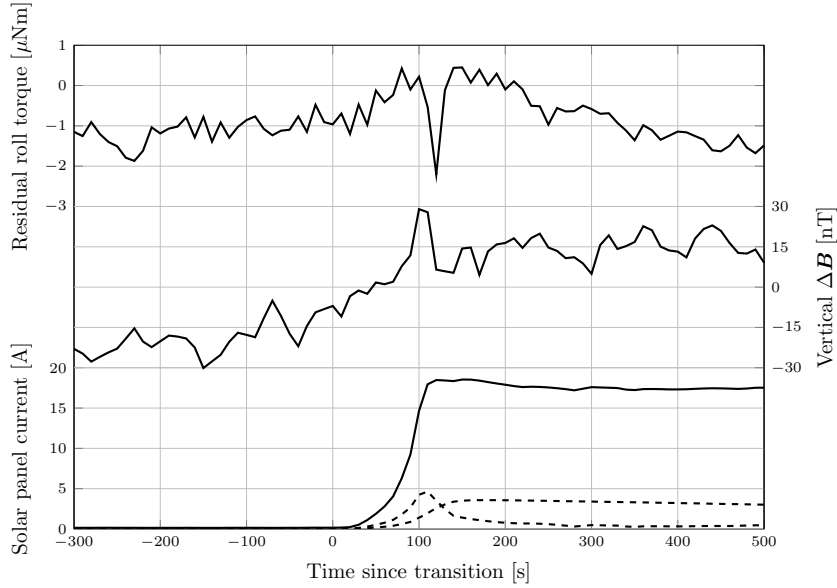


Figure 13: Residual roll torque, vertical magnetic field deviation from IGRF, and current from the solar panels (total (solid line) and two examples out of six panels (dashed lines)), as a function of the time since the transition out of eclipse on April 11, 2011, around 5:15 UTC.

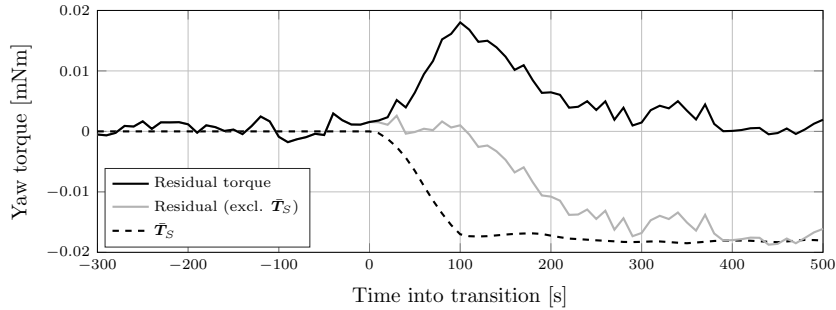


Figure 14: Residual yaw torque (black solid line), the residual excluding solar radiation pressure ($\mathbf{T} - (\mathbf{T} - \mathbf{T}_S)$, gray solid line), and the solar radiation pressure model itself (\mathbf{T}_S , dashed line) versus the time into transition on the second orbit of April 8, 2011. The eclipse transition model is two to three times faster than the actual transition out of eclipse, causing a bump in the residual torque.

the month, with a minimum at -0.998. This result implies that the documented dipole has the wrong sign. After inverting the documented model, we inspected all jumps in thrust due to maneuvers over the entire mission. Taking the 65 jumps for which all required data is available, a linear fit is estimated between the modeled and observed jump in both force and torque. For the observation the difference between the measurement and all other models ($\mathbf{T} - (\bar{\mathbf{T}} - \bar{\mathbf{T}}_I)$) is used. A good fit is found for force in the x_B - and z_B -direction (coefficient of determination (R^2) above 0.99), with a linear term of 1.038 and 1.022 respectively. This implies that the error in the commanded thrust that is used in the model is indeed within the documented 5% (Kolkmeier et al., 2008). For the pitch and yaw torques linear terms of 0.21 and 0.52 are found respectively (R^2 around 0.84). This mismatch can be explained by a combination of a rotation and repositioning of the thruster, but may also be affected by an error in the thruster dipole model. This process has many solutions within the documented error constraints, so no conclusion can be drawn regarding the actual position and orientation of the thruster. Therefore the model is kept as documented.

In the residual pitch torque a band of large errors is found around the South pole in the local winter months and other situations where the thermosphere neutral density is very low. At those instances the thrust level passes through a band around 2mN in which the thruster noise is significantly larger at around 5% (Wallace et al., 2011). In the case of the pitch torque it is not the thruster itself, but its main magnet that is causing the error. Attempts to estimate a scale factor for this dipole as was done for the torquers (described in Section 3.6) have however not given consistent, reliable results. Therefore the thruster dipole torque is only considered validated for thrust levels above 3mN. Given GOCE's orbit, with the apogee over the South pole, thrust levels below this threshold occur mostly over the South pole during local winter, but have also been observed over the North pole. In the last year of the mission, when solar activity increases and the orbit is lower, the thrust remains above the threshold under nominal conditions.

4.6. Constant dipoles of spacecraft bus and payload

As not all dipoles are known, it is impossible to validate the torque they cause. Instead the trend of the fitted dipoles over time is investigated. As only constant dipoles were estimated, they should not vary more than can be explained by aging or hardware being switched on or off. The downside of comparing dipoles is that the estimation process in Eq. (15) does not

have a unique solution. A different dipole therefore does not always imply a different torque. This effect is eliminated for most parameters by estimating a single set of dipoles using one full day of torque data. Only the diagonal components of the soft magnetic dipole do not have a unique solution, as explained in Section 3.6.

In Fig. 4 the daily estimates of hard and soft magnetic dipoles are plotted for the full mission. The hard magnetic dipole is similar in scale and opposite in sign to the bus dipole in the y_B and z_B axes (Kolkmeier et al., 2008, cf.). In x_B the sign is the same, but the estimated dipole is approximately five times as small as the bus dipole. All elements remain mostly constant over the first three years of the mission. The linear fit predicts a decrease in magnitude of 0.05 Am^2 per year with a small overall prediction error (see Table 5). In the last year the x_B and z_B components show a stronger increasing trend, which can also be observed in some elements of the soft magnetic dipole, the magnetic torquer factors, and the estimated offsets. This episode starts with the end of the orbit-lowering maneuver of August 2012, but the cause of this behavior is unclear.

The hard magnetic dipole that is estimated for episodes in which both GPS receivers are turned on (highlighted in light gray in the top row of Fig. 4) shows a stronger linear trend than the nominal estimated dipole. As this linear fit is dominated by a large set of data in the last months of the mission, this confirms the observed increasing trend in the hard magnetic dipole described above.

The diagonal soft magnetic elements (row 2–4 of Fig. 4) are of similar scale as those reported for the spacecraft bus, while documented off-diagonal elements are generally two orders of magnitude smaller. They display similar consistency as the hard magnetic dipoles (see Table 5), except for those related to the cross-track component of the magnetic field (middle column). This can be explained by the fact that this component of the field is generally small throughout the (near-polar) orbit, leading to a high parameter variance.

The co-estimated offsets in the torques, plotted at the bottom of Fig. 4, oscillate around the linear trend in the roll and yaw axes. In pitch the offset assumes a more profound increasing trend after the orbit maneuver in August 2012. This behavior explains the large error in the linear fit reported in Table 5.

Table 5: The root mean square error with respect to the linear fit of each estimated parameter, as a percentage of the maximum L^2 -norm of the vector or matrix it is an element of.

	x_B	y_B	z_B
Hard dipole $\hat{\boldsymbol{\mu}}_{P,H}^T$	4.5%	2.1%	2.8%
	6.0%	23.4%	6.9%
Soft dipole $\hat{M}_{P,S}$	1.8%	5.2%	1.4%
	7.9%	12.9%	3.0%
Torquer factors \hat{S}_T	10.4%	31.5%	13.8%
	2.2%	15.8%	4.6%
	6.8%	15.7%	15.9%
Torque offset $\hat{\mathbf{T}}_{off}^T$	3.6%	34.4%	41.3%

4.7. Complete model

To evaluate the validity of the complete model, the residual is analyzed for the period in May 2011 plotted in Fig. 8. In Table 6 the standard deviation (STD) of the residual is provided. To make a fair comparison with the actual torque acting on the satellite around each principle axis, the values are divided by the STD of the control torque acting on the satellite around that axis. This results in the relative standard deviation. To complete the table a column is added for the mean value of the residual, or the overall bias of the models. This value is again normalized with the STD of the control torque to find the relative bias.

From the table we find that the yaw residual has the largest relative value. Given the large aerodynamic signal in this direction, this result implies that especially the aerodynamic model requires improvement. The small residual in pitch indicates that the magnetic dipole models are performing well.

An error in the star camera alignment may cause part of the residual through the aerodynamic, gravity gradient, and radiation pressure models. For the EGG_IAQ attitude product an error with standard deviation $3''$ is to be expected around all axes (Stummer, 2012). A random normal noise signal with this standard deviation is added to the attitude (in case of the gravity gradient torque) or incidence angles to obtain the maximum expected error in the torque around each axis. The root mean square (RMS) of this difference does not exceed 1×10^{-6} mNm in roll, 2×10^{-4} mNm in pitch, and 3×10^{-5} mNm in yaw. Comparing these RMS values to the STD values

Table 6: Standard deviation (STD) and bias of the residual torque over the period plotted in Fig. 8, both absolute and relative (Rel.) to the STD of the control torque about the same axis.

	STD [mNm]	Rel. STD [%]	Bias [mNm]	Rel. bias [%]
roll	2.51e-03	15.6	-1.51e-03	-9.4
pitch	7.25e-03	2.1	-1.14e-03	-0.3
yaw	1.67e-02	30.5	1.09e-02	19.9

reported in Table 6, we find that the effect of uncertainty in the attitude on the residual torque is negligible.

5. Discussion and conclusion

In this paper a set of models was presented that together predict the torque acting on the GOCE satellite, based on its full state (spatial and rotational), the local magnetic field, the currents running through the thruster magnet and magnetic torquers, and the applied thrust force. The accuracy of the result depends heavily on the accuracy of the dominant torque, which is different around each body axis.

In the roll direction errors of 15% are to be expected (in terms of the relative standard deviation, see Table 6). The residual torque, as displayed in Fig. 8a, shows clear periodic patterns that resemble magnetic torques. It is possible that the weighting scheme for the payload dipole estimation (see Section 3.6) prioritizes the residuals in pitch and yaw torque, because of their larger overall scale.

In pitch the expected errors are smallest, at around 2%. This low number is partially due to the large control torque in this direction, which is meant to balance the (mostly constant) residual dipole of the bus and payloads. The dominant trend in the residual is caused by an error or noise signal in the current running through the thruster main magnet when thrust is close to the 2mN level. This generally occurs in low density conditions, i.e. early in the mission, mostly over the South Pole in local winter conditions.

The yaw error is largest of the three, with relative standard deviation running up to and over 30%. Throughout the mission the yaw residual is positive over the Northern hemisphere, and negative over the Southern hemisphere. This suggests an error in the neutral density, as the perigee of the (near-circular) orbit lies close to the North Pole. At the same time the North

and South magnetic poles show up as bands of large residuals, that increase in magnitude during magnetic storms. This implies that the (effect of) wind is not modeled properly. Together the above two observations leave us to conclude that a mismatch exists between the aerodynamic model from AN-GARA and the thermospheric density and wind data derived using a panel model. The errors in the aerodynamic model and thermospheric data together cause most of the residual in the yaw direction.

The current study shows that it is vitally important to have a complete model of the magnetic properties of a satellite, in addition to the aerodynamic models, in order to fully characterize the torques it is subject to. To improve the torque models beyond the level presented here, one would for instance require the magnetic dipole caused by electric currents from the solar panels. Parameters of such a model can be estimated in post processing, as described in Section 3.6, but a full magnetic characterization before launch would most likely reduce the uncertainty levels. Such a characterization would certainly be needed for future missions that would use both force and torque analyses for the investigation of satellite aerodynamics and thermosphere dynamics, and the absence of such a characterization would be problematic in applying data from current or past missions for this purpose.

We expect that the effect that causes the largest errors in the torque models largely depends on the satellite and mission design. Most LEO satellites are in a significantly higher orbit than GOCE was, reducing the aerodynamic torque and therefore its relevance as an error source. Therefore the magnetic model errors are expected to dominate the residual torque on satellites like GRACE and CHAMP. Both carry magnetic torquers that may have uncertainty margins like those installed on GOCE (see Section 3.1). As is the case for GOCE, electric currents from solar panels or towards equipment with a high current demand will most likely also show up in the residual torque. For a mission like Swarm, where the satellites are designed to be magnetically clean and there is no continuous thrusting like on GOCE, the solar radiation pressure model could be the main error source. Because of its low sensitivity to model errors, it is unlikely that the gravity gradient torque is a significant source of error for any LEO satellite.

Returning our attention to the GOCE analysis, the aerodynamic signals in the yaw residuals provide an opportunity to improve the aerodynamic model and the thermospheric horizontal wind data. Moreover, comparing Fig. 8b and 8c we observe that a similar signal is present around the North magnetic pole in the pitch residual. This signal may well provide vertical

wind data. Our goal for future work is to extract these wind signals from the residual torque and combine the result with that obtained from the linear accelerations to find a consistent wind data set and consistent aerodynamic model parameters.

Recent efforts to obtain angular accelerations from the star tracker attitude quaternions only, so without making use of GOCE's accelerometers, show promising results. In the angular acceleration data derived from the star trackers, the large-scale wind patterns can be observed. Therefore we are considering a similar torque modeling and wind extraction effort for the Swarm satellites, and it would be worth investigating the feasibility of applying such a thermosphere wind extraction processing approach as well to much simpler mission concepts, such as star-tracker carrying CubeSats.

Acknowledgements

The authors would like to thank Rune Floberghagen, Björn Frommknecht and Michael Fehringer at ESA for their help in accessing the GOCE data (access may be requested at <https://earth.esa.int/web/guest/-/goce-data-access-7219>) and documentation (available upon personal request to ESA) used for this research. We also thank NASA's Langley Research Center for maintaining the CERES data, available at <https://ceres.larc.nasa.gov/products.php?product=SYN1deg>.

6. References

- Bandikova, T., Flury, J., Ko, U.-D., July 2012. Characteristics and accuracies of the GRACE inter-satellite pointing. *Advances in Space Research* 50 (1), 123 – 135.
- Cometto, F., April 2007. GOCE Models Data Bank. Tech. Rep. GO-TN-AI-0081_6, Alenia Spazio.
- Dhadly, M., Emmert, J., Drob, D., Conde, M., Doornbos, E., Shepherd, G., Makela, J., Wu, Q., Niciejewski, R., Ridley, A., Feb. 2017. Seasonal dependence of northern high-latitude upper thermospheric winds: A quiet time climatological study based on ground-based and space-based measurements. *Journal of Geophysical Research: Space Physics* 122 (2), 2619–2644.

- Doornbos, E., March 2011. Thermospheric Density and Wind Determination from Satellite Dynamics. Ph.D. thesis, Delft University of Technology.
- Doornbos, E., July 2016. GOCE+ Theme 3: Air density and wind retrieval using GOCE data: Data Set User Manual.
URL https://earth.esa.int/documents/10174/679909/GOCEPlus_Theme_3_Dataset_User_Manual
- Doornbos, E., Foerster, M., Fritsche, B., Van Helleputte, T., van den IJssel, J., Koppenwallner, G., Lühr, H., Rees, D., Visser, P., 01 2009. ESTEC contract 21022/07/NL/HE air density models derived from multi-satellite drag observations - Final report, 7–39.
- Doornbos, E., van den IJssel, J., Lühr, H., Förster, M., Koppenwallner, G., July-August 2010. Neutral Density and Crosswind Determination from Arbitrarily Oriented Multiaxis Accelerometers on Satellites. *Journal of Spacecraft and Rockets* 47 (4), 580–589.
- Drinkwater, M. R., Floberghagen, R., Haagmans, R., 2003. GOCE: ESA's first Earth Explorer Core mission. In: *Earth gravity field from space - from sensors to Earth sciences*. Space Sciences Series of ISSI. pp. 419–432.
- Dumontel, M., April 2010. GOCE Stand-alone Aerodynamic Model How-to. Tech. Rep. GO-TN-AI-0179, ThalesAlenia Space.
- Emmert, J., Sep. 2015. Thermospheric mass density: A review. *Advances in Space Research* 56 (5), 773–824.
- Fehringer, M., Andre, G., Lamarre, D., Maeusli, D., Feb. 2008. A jewel in ESA's crown. *ESA bulletin*, 14–23.
- Floberghagen, R., Fehringer, M., Lamarre, D., Muzi, D., Frommknecht, B., Steiger, C., Piñeiro, J., da Costa, A., Nov 2011. Mission design, operation and exploitation of the gravity field and steady-state ocean circulation explorer mission. *Journal of Geodesy* 85 (11), 749–758.
- GOCE Flight Control Team (HSO-OEG), Feb. 2014. GOCE End-of-Mission Operations Report. Tech. Rep. GO-RP-ESC-FS-6268.
- Kärräng, P., 2015. Comparison of thermospheric parameters from space- and ground- based instruments. Master's thesis, Luleå University of Technology.

- King-Hele, D., 2005. A tapestry of orbits. Cambridge University Press.
- Kolkmeier, A., Präger, G., Möller, P., Strandberg, T., Kempkens, K., Stark, J., Gessler, L., Hienerwadel, K. O., April 2008. GOCE - DFAC Interface Control Document. Tech. Rep. GO-IC-ASG-0005_12, EADS Astrium.
- Koppenwallner, G., Nov. 2008. Comment on Special Section: New Perspectives on the Satellite Drag Environments of Earth, Mars, and Venus. *Journal of Spacecraft and Rockets* 45 (6), 1324–1327.
- Mehta, P. M., Walker, A., Lawrence, E., Linares, R., Higdon, D., Koller, J., 2014. Modeling satellite drag coefficients with response surfaces. *Advances in Space Research* 54 (8), 1590 – 1607.
- Mehta, P. M., Walker, A. C., Sutton, E., Godinez, H. C., Jan. 2017. New density estimates derived using accelerometers on-board the CHAMP and GRACE satellites. *Space Weather* 15 (4), 558–576.
- Pilinski, M. D., Argrow, B. M., Palo, S. E., Bowman, B. R., May 2013a. Semi-Empirical Satellite Accommodation Model for Spherical and Randomly Tumbling Objects. *Journal of Spacecraft and Rockets* 50 (3), 556–571.
- Pilinski, M. D., Moe, K., Palo, S. E., Argrow, B. M., Mar. 2013b. Measuring Absolute Thermospheric Densities And Accommodation Coefficients Using Paddlewheel Satellites: Past Findings, Present Uses, And Future Mission Concepts. *The Journal of the Astronautical Sciences* 58 (3), 531–549.
- Roithmayr, C. M., January 1991. Contribution of zonal harmonics to gravitational moment. *Journal of Guidance, Control, and Dynamics* 14 (1), 210–214.
- Rummel, R., Yi, W., Stummer, C., Aug 2011. Goce gravitational gradiometry. *Journal of Geodesy* 85 (11), 777.
- Siemes, C., Jan 2018. Improving goce cross-track gravity gradients. *Journal of Geodesy* 92 (1), 33–45.
- Stummer, C., October 2012. Gradiometer Data Processing and Analysis. Ph.D. thesis, Institut für Astronomische und Physikalische Geodäsie.
- Sutton, E. K., Jan. 2009. Normalized Force Coefficients for Satellites with Elongated Shapes. *Journal of Spacecraft and Rockets* 46 (1), 112–116.

- Visser, P., Doornbos, E., van den IJssel, J., Teixeira da Encarnação, J., Nov 2013. Thermospheric density and wind retrieval from swarm observations. *Earth, Planets and Space* 65 (11), 12.
URL <https://doi.org/10.5047/eps.2013.08.003>
- Walker, A., Mehta, P., Koller, J., Sep. 2014. Drag Coefficient Model Using the Cercignani–Lampis–Lord Gas–Surface Interaction Model. *Journal of Spacecraft and Rockets* 51 (5), 1544–1563.
- Wallace, N., Jameson, P., Saunders, C., Fehringer, M., Edwards, C., Floberghagen, R., September 11-15 2011. The GOCE ion-propulsion assembly - lessons learnt from the first 22 months of flight operations. In: 32nd International Electric Propulsion Conference, Wiesbaden, Germany.
- Wertz, J. R., 1978. *Spacecraft attitude determination and control*. Kluwer.
- Wie, B., 2008. *Space Vehicles Dynamics and Control*. American Institute of Aeronautics and Astronautics.